Journal of
Nanoelectronics and Optoelectronics
Vol. 3, 1–21, 2008

REVIEW

Simulation of Heat Conduction in Suspended Graphene Flakes of Variable Shapes

Samia Subrina* and Dmitri Kotchetkov

Department of Electrical Engineering, University of California–Riverside, Riverside, CA 92521, USA

Graphene is a novel material that reveals many remarkable properties. Academic and industry research groups around the globe are carrying out theoretical and experimental studies to discover and investigate characteristics of graphene. Due to its outstanding properties, graphene has a potential to revolutionize technology. Particularly, graphene was found to be one of the best known heat conductors [Balandin et al., Nano Lett. 8, 902 (2008)], which suggests that it can be used in nanoelectronic and optoelectronic devices as a heat spreader component. The extremely high thermal conductivity was found for single layer graphene, which consisted of one crystalline plane of sp^2-bound carbon atoms. In that experiment a method of measuring G peak position of the Raman spectrum as a function of both the temperature of the graphene sample and the power of the heat source was used to compute the thermal conductivity. The sample in the experiment had approximately rectangular geometry and a simple model was used to extract the thermal conductivity under certain assumptions about the nature of the thermal transport. In this work we used finite-element simulations to model the heat spreading in graphene flakes of variable shapes. We also investigated how the thermal transport is influenced by the geometry of the heat source and flake width. We found that all mentioned factors impact heat propagation and have to be included in the experimental data extraction. The simulations also proved that for the rectangular geometry of the flake and specific conditions of the experiment, e.g., ratio of the flake width to the laser spot size, the simple one-dimensional model data extraction was adequate. The developed simulation procedure can be further used for investigation of thermal transport in graphene multi-layers and graphene–heat sink structures. The latter is required in order to study the feasibility of application of graphene multi-layers for the lateral hot-spot removal and other device-level thermal management applications.

Keywords: Heat Conduction, Graphene, Simulation, Thermal Conductivity.

CONTENTS

1. UNIQUE CHARACTERISTICS OF GRAPHENE

Graphene is a recently discovered material[1,2] in which carbon atoms are arranged in sp^2 planar hexagonal sheet structure. Such structure is a building element for any graphitic material, for example, graphite represents an ensemble of stacked graphene sheets. Graphene possesses some unique properties that make it a very promising material for electronic devices and circuits. In most conductors and semiconductors electron transport can be described by non-relativistic quantum equations. But in graphene electrons and holes behave like relativistic particles.[3] The E–k relation is linear at low energies near six corners of the two-dimensional hexagonal Brillouin zone. That leads to zero effective masses for electrons and holes that can be described by the Dirac equation for spin 1/2 particles. Experimental results and simulations suggest that graphene has very high values of electron mobility at room temperature. Intrinsic mobility can reach the value[4] as high as 2×10^5 $cm^2V^{-1}s^{-1}$ at a carrier density of 10^{12} cm^{-2}. For such a case, the corresponding resistivity of the graphene sheet would be 10^{-6} Ohm-cm, which is slightly less than the resistivity of silver (1.6×10^{-6} Ohm-cm), the least resistive metal. The magnitude

*Author to whom correspondence should be addressed.

of an electron mobility of graphene exceeds that of InSb (7.7×10^4 $cm^2V^{-1}s^{-1}$) and is comparable to an electron mobility of carbon nanotubes (1×10^5 $cm^2V^{-1}s^{-1}$). A single layer graphene has an opacity which is unexpectedly high for just one atomic layer. The white light absorption is

$$\pi\alpha = 2.3\% \tag{1}$$

where α is the fine-structure constant.[5,6] Graphene is a very strong and rigid material. If several layers of graphene are suspended over cavities, graphene sheets are held together by van der Waals forces and one can measure mechanical properties of the suspended sheet using an atomic force microscope.[7] The spring constant and Young's modulus of graphene were found to be 1–5 N/m and 0.5 TPa, correspondingly. Such remarkable elastic properties could lead to utilization of graphene as a material for sensors and resonators.

Graphene might be the first observed two-dimensional crystal. However, it is still debated whether such a statement is true. Mermin-Wagner theorem states that continuous symmetries cannot be spontaneously broken at finite temperature in one- or two-dimensional theories.[8–10] In other words, a two-dimensional crystal cannot remain ordered in a three-dimensional environment, because of long wavelength fluctuations. The theorem leads to an assumption that a large two-dimensional structure will eventually fold or collapse into a more stable three-dimensional crystal. Graphene has a tendency to ripple,[11] if suspended. Such tendency, in part, supports the Mermin-Wagner theory. Proponents for a truly two-dimensional structure of graphene argue that the Mermin-Wagner theorem is applicable for infinite structures, or, at least, for layers with very large sizes, but finite-size graphene layers can remain stable as two-dimensional crystals. In the presence of a magnetic field graphene shows an anomalous quantum Hall effect.[2] The Hall conductivity of a single layer graphene is

$$\sigma_{xy} = \mp\frac{4e^2\left(N+\frac{1}{2}\right)}{h} \tag{2}$$

where h is the Plank constant, e is the elementary charge, and N is the Landau index level. The factor 4 comes from double valley and double spin degeneracies. Above equation shows that the sequence is shifted by 1/2 from the standard. Contrary to single layer graphene, bilayer graphene displays the quantum Hall effect but the sequence is standard:

$$\sigma_{xy} = \mp\frac{4Ne^2}{h} \tag{3}$$

In presence of very intense, time varying magnetic fields the conductivity of graphene oscillates. This is so-called

Samia Subrina received her B.S. degree in Electrical and Electronic Engineering from the Bangladesh University of Engineering and Technology (BUET) in 2003. She received her M.S. degree from the same department in 2006 with a specialization in optoelectronic devices. After graduation she worked at the Department of Electrical and Electronic Engineering in BUET as a Lecturer. She joined Professor Balandin's Nano-Device Laboratory at the Department of Electrical Engineering of the University of California–Riverside (UCR) in 2007. Currently she is working toward her Ph.D. degree focusing on modeling and simulation of graphene materials and devices. Her research interests include modeling, simulation and characterization of nanostructured materials; thermal transport in graphene; thermal management of nanscale devices; and luminescence properties of optoelectronic materials and devices. She is a student-member of the FCRP Center on Functional Engineered Nano Architectonics (FENA) at UCLA.

Dmitri Kotchetkov received M.S. degree in Electro-Mechanical Engineering from the Moscow State Technical University named after N.E. Bauman in 1994 and M.A. degree in Law from the Moscow State Law Academy in 1997. From 1994 to 1997 he worked in Moscow, Russia as a project manager of electronic and mechanical security systems. He moved to the United States in 1997 and received M.S. degree in Electrical Engineering in 2002, M.S. degree in Physics in 2003, and Ph.D. degree in Physics in 2005, all from the University of California, Riverside. From 1998 to 2008 he had worked on two major nuclear and particle physics experiments, PHENIX at Brookhaven National Laboratory and ATLAS at CERN (European Center for Nuclear Research), participating in detector construction and commissioning, software development and experimental data analysis. He joined Professor Balandin's Nano-Device Laboratory at the Department of Electrical Engineering, University of California–Riverside in 2008. Currently he is primarily interested in experimental studies of electrical and thermal properties of carbon-based materials. He is a member of American Physics Society and Sigma Xi, The Scientific Research Society. He authored more than 80 publications on nuclear and particle physics, material science, physics detectors and security systems.

Shubnikov-de Hass effect. The longitudinal resistance of graphene is at maximum[12] for every Landau index value N. This is an opposite to many metals, since they show the minimum of resistance for the integral Landau values N. A possible explanation of such phenomenon could be Berry phase that occurs due to zero effective masses of the carriers near Dirac points.[13] Although E–k relation manifests zero carrier masses, studies of Shubnikov-de Hass oscillations as a function of temperature reveals that the carriers in graphene have non-zero cyclotron masses.[12]

Unique mechanical and electromagnetic properties make graphene a very promising material for a variety of high-tech applications. Particularly, due to a very high conductivity, graphene can be used to fabricate ballistic field-effect transistors and integrated circuits. Graphene can be utilized in single molecule gas sensors; absorption of just one molecule drastically changes a local electrical resistance. Nanoribbons with specific electrical properties can be made of graphene to be used in interconnects. High optical transparency, mechanical strength and flexibility allow use of graphene in transparent conducting electrodes such as liquid crystal displays, organic photovoltaic cells and touchscreens.

2. THERMAL CONDUCTIVITY OF SINGLE LAYER GRAPHENE

Besides its outstanding electromagnetic and mechanical properties, graphene shows unique thermal characteristics. The room temperature thermal conductivity of graphene was discovered to be extremely high.[14, 15] Recent experimental observations by Balandin et al.[14] suggested the graphene thermal conductivity to be within the range from 3080 $Wm^{-1}K^{-1}$ to 5300 $Wm^{-1}K^{-1}$. This values substantially exceed those of diamond (1000–2200 $Wm^{-1}K^{-1}$) which to date is considered to be the best bulk thermal conductor. The values extracted for graphene are on the upper bound of those reported for carbon nanotubes or exceed them. At the same time one should keep in mind the ambiguity of defining the thermal conductivity for a single atomic layer due to the uncertainty of the atomic layer thickness. Outstanding heat transport properties of graphene make it a promising material for heat management for semiconductor devices and circuits. One can use ultrathin films of graphene as heat spreading components or embed graphene in some other materials to increase overall thermal conductivity. Moreover, if graphene is used as a material for interconnects, it not only allows faster gate switching, but also efficiently removes the heat from the regions of ultra high device integration.

The measurement of the graphene thermal conductivity[14, 15] was preceded by investigation of its Raman spectrum.[16] In that experiment a single layer graphene was exfoliated from bulk graphite and placed on a silicon substrate covered with a film of SiO_2. Using Raman spectrometer the graphene layer was excited with visible (488 nm) laser light, and the backscattering data were collected. A cold-hot cell operated using liquid nitrogen was able to control the temperature of the sample, which was varied from −190 °C to 100 °C. The position of the G peak in the spectrum was measured and found to be changing from ∼1584 cm^{-1} to ∼1578 cm^{-1}. The resulting G peak position distribution was fitted with the user-defined linear function[16]

$$\omega = \omega_0 - \chi T \tag{4}$$

where the temperature coefficient $\chi = 0.016$ $cm^{-1}K^{-1}$.

The very fact that the G peak position strongly depends on temperature allowed for the designing and carrying out the experiment during which the thermal conductivity of graphene was measured for the first time (see Fig. 1). In that experiment a trench with the width of ∼2–5 μm was made on the Si/SiO_2 substrate by reactive ion etching. The thickness of SiO_2 layer (the depth of the trench) was ∼300 nm. A single layer graphene flake was placed across the trench. Then the laser light from Raman spectrometer was focused in the middle of the suspended flake with the spot size of about 0.5–1.0 μm. Large graphitic pieces were placed on top of the graphene flake at the distance of 10 μm from the trench edges. Those graphitic pieces acted as heat sinks. The temperature of the heat sinks was constant and equal to ambient room temperature. Power from the laser light was dissipated in the flake. Due to the low thermal conductivities of air and SiO_2 it was reasonable to assume that the heat dissipation into the air and SiO_2 was negligible, so the heat was propagating laterally within the flake from the laser spot toward the

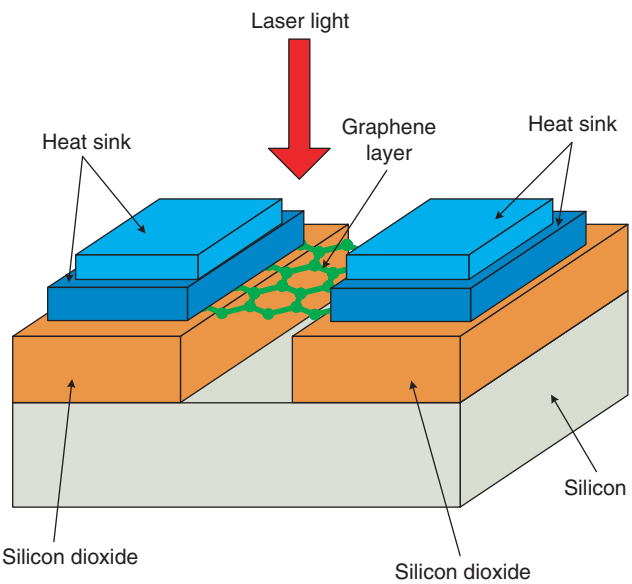

Fig. 1. Experimental setup for measurement of thermal conductivity of graphene.

heat sinks. Excitation power was controlled and varied, and the G peak position of the Raman spectrum was measured in regard to a particular value of the power. Thus the G peak position was extracted as a function of the power dissipated in graphene.

Heat propagation in graphene occurs through conduction. Conduction is defined as a spontaneous transfer of thermal energy from a region with high temperature to a region with low temperature. Direct molecular (or atomic) interactions are involved in the heat conduction either within the same medium or between different media if they are in physical contact. The heat propagation in graphene is mostly due to acoustic phonons (atomic vibrations).[15] The law of heat conduction defines the time rate of heat transfer as

$$\frac{\partial Q}{\partial t} = -k \oint \vec{\nabla} T \cdot \overrightarrow{dS} \tag{5}$$

where $\partial Q/\partial t$ is the heat transfer rate, i.e., amount of heat transferred per unit time, [W], T is the temperature, [K], S is the surface through which the heat is flowing, [m^2], and k is the thermal conductivity, [$Wm^{-1}K^{-1}$]. This equation means that the heat transfer rate is proportional to the negative gradient in the temperature and to the area of the surface through which the heat is flowing. That surface is normal to the temperature gradient. This allows us to write the heat conduction equation as

$$\frac{\partial Q}{\partial t} = -k \frac{dT}{dX} \vec{X} \cdot \vec{x} \oint dS \tag{6}$$

where x is the magnitude of the unit vector normal to the surface through which the heat is flowing. The minus sign in the equation indicates that the temperature drops along the direction of the heat flow. We drop the minus sign from further equation transformations.

To extract the thermal conductivity of single layer graphene the flake was thought to be a parallelepiped (a rectangle if viewed from top). The axes of Cartesian coordinate system are orthogonal to the surfaces of the flake. Thus

$$\frac{\partial Q}{\partial t} = k \frac{dT}{dX} \int_0^W dy \int_0^h dz \tag{7}$$

or

$$P = k \frac{dT}{dX} Wh \tag{8}$$

where $P = (\partial Q/\partial t)$, which is equal to the heat power dissipated in the flake (or the heat transfer rate), W is the width of the flake, [m], h is the thickness of the flake, [m], and Wh is the cross-sectional area of the flake, [m^2]. If the diameter of the laser sport is comparable to the width of the graphene flake, to simplify the solution, one can approximate the shape of the heat source into an infinitesimally thin line, the length of which equals the width of the modeled flake. A graphene layer has a thickness of one carbon atom plane (~0.35 nm). Since it is rather thin, heating the top plane of the flake with the hot line can be seen as resulting in creating within the flake a uniformly

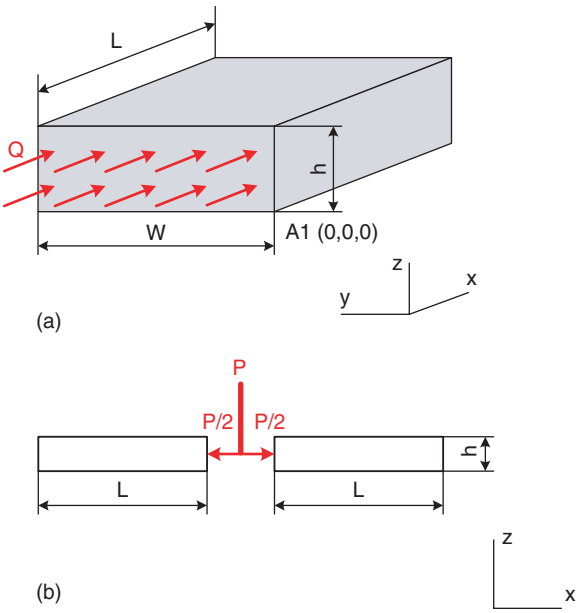

Fig. 2. (a) Half-flake of single layer graphene. (b) Representation of the heat flow in graphene as heating two adjacent identical half-flakes.

hot surface normal to the flake's plane. The length of this hot surface is equal to W and the width of this surface is equal to 0.35 nm.

If one cuts imaginarily the parallelepiped flake along the line of the heat source into two pieces (half-flakes), for each piece the heat can be seen as flowing into the half-flake through surfaces (intake surfaces). These surfaces both pass through three points: $A_1 = (0, 0, 0)$, $A_2 = (0, W, 0)$ and $A_3 = (0, 0, h)$ (see Fig. 2). The plane that passes through the points $A_4 = (L, 0, 0)$, $A_5 = (L, W, 0)$ and $A_6 = (L, 0, h)$ for one half-flake and the plane that passes through the points $A_7 = (-L, 0, 0)$, $A_8 = (-L, W, 0)$ and $A_9 = (-L, 0, h)$ for the other half-flake are connected to heat sinks, so the temperatures of those planes (sink planes) are constant (note that $2L$ is the length of the flake). All other surfaces of the half-flakes are assumed to be perfectly insulated from the surroundings. If one considers the half-flake, the fact that (1) the half-flake has a parallelepiped shape, (2) one of the surfaces is thermally connected to a heat sink, and (3) all surfaces, except for the intake and sink planes, are thermally insulated leads to considering the temperature in the half-flake as linearly changing, thus we can replace the derivative dT/dx with $\Delta T/\Delta x$ and write

$$\frac{P}{2} = k \frac{\Delta T}{\Delta x} Wh \tag{9}$$

In the Eq. (9) the dissipated power P is divided by 2, since the suspended graphene flake was heated in the middle and we considered the heat propagation as two equal and opposite flows going through the identical adjacent half-flakes (note that $\Delta x = L$). Changes in the dissipated power result in changes in the temperature of the intake

surface. The temperature of the sink surface remains constant at 300 K. Thus for a particular value of the dissipated power there is one unique temperature of the intake surface:

$$\frac{P_1}{2} = k\frac{\Delta T_1}{\Delta x_1}Wh = k\frac{T_1 - T_s}{L}Wh \tag{10}$$

$$\frac{P_2}{2} = k\frac{\Delta T_2}{\Delta x_2}Wh = k\frac{T_2 - T_s}{L}Wh \tag{11}$$

where T_s is the temperature of the heat sink. We can express the change in the power as

$$P_2 - P_1 = k\frac{2(T_2 - T_1)}{L}Wh \tag{12}$$

and the thermal conductivity as

$$k = \frac{L(P_2 - P_1)}{2Wh(T_2 - T_1)} \tag{13}$$

The G peak position of Raman spectrum was found to be linearly dependent on temperature

$$\delta T = \frac{\delta\omega}{\chi} \tag{14}$$

where $\delta\omega$ is the shift in G peak position in Raman spectrum, $[m^{-1}]$, and χ is the temperature coefficient, $[m^{-1}K^{-1}]$. This allows one to write the thermal conductivity of the parallelepiped graphene flake as

$$k = \left(\frac{L}{2Wh}\right)\cdot\chi\left(\frac{\delta\omega}{\delta P}\right)^{-1} \tag{15}$$

During the experiment[14, 15] the power variations δP were relatively small. The G-peak position in the Raman spectrum was shifted linearly depending on how the dissipated power was changing. For the Raman spectrum with the excitation wavelength of 488 nm, the spectrometer power was varied from 0.5 mW to 4 mW. The G-peak position was found to be

$$\omega = \omega_0 - \theta P_D \tag{16}$$

where $\theta = 1.226\ cm^{-1}(mW)^{-1}$ and P_D is the power of the spectrometer (detector). Only a fraction of P_D can be dissipated in graphene:

$$P = \eta P_D \tag{17}$$

where $\eta = 0.11$–0.13. This was found through a special calibration procedure.[15]

Finally the thermal conductivity of the parallelepiped (rectangular if viewed from top) single layer graphene flake can be expressed as

$$k = \left(\frac{\eta L}{2Wh}\right)\cdot\chi\left(\frac{\delta\omega}{\delta P_D}\right)^{-1} \tag{18}$$

or

$$k = \left(\frac{\eta L}{2Wh}\right)\cdot\chi\theta^{-1} \tag{19}$$

Equation (19) defines the thermal conductivity of the flake which has a rectangular shape. In reality, the flake's shape can deviate from a simple rectangle. In the experiments[14, 15] the single layer graphene thermal conductivity was found to be in the range of 3080 $Wm^{-1}K^{-1}$ to 5300 $Wm^{-1}K^{-1}$. From these results the average temperature of a graphene flake was estimated to be ~370–400 K.

3. SIMULATING HEAT PROPAGATION IN GRAPHENE

The experiment measured the thermal conductivity of graphene to be within a relatively wide range. During the derivation of the thermal conductivity two major assumptions were made among others (i) the shape of the flake was thought to be rectangular; (ii) the size of the laser spot was comparable to the width of the flake so that the spot was approximated to be seen as a line heat source producing a plane front of the heat. It is clear that the future experiments have to examine the effects of the flake's shape and geometry of the heat source on the measured value of the thermal conductivity. Such systematic studies might not only improve an accuracy of the thermal conductivity measurements but also help understand a picture of the heat propagation in graphene. Meantime, simulations can be performed to study the above mentioned affects. We simulated the heat propagation in single layer graphene and studied various shapes and heat sources. The main objective of the simulation was to model the heat propagation in graphene for different geometries of the flake and the heat source and to see whether the simulated values of the thermal conductivity fall within the experimental range. Also, simulating different geometries of the flake and the heat source allows us to study how they can affect calculations of the thermal conductivity. This eventually helps plan future experiments.

We simulated the heat propagation in graphene using COMSOL Multiphysics software package.[17] COMSOL package is a finite element analysis tool and it has application-specific modules for various physics phenomena: AC/DC Module, Acoustic Module, Structural Mechanics Module, Heat Transfer Module and others. The finite element analysis technique is a numerical method for finding approximate solutions of partial differential equations. The solutions are mostly based on dividing the simulated object into a large set of very small components and linearizing the differential equations within each of the components.

To simulate the heat propagation in graphene we created three models which differ from each other primarily by types of the heat sources:

(i) the model of the line heat source,
(ii) the model of the disk heat source, and
(iii) the model of the Gaussian heat source.

In COMSOL the design of the model involves several steps that include

REVIEW

(1) object's geometry specification,
(2) division of the object into subdomains,
(3) description of every subdomain,
(4) specification of subdomains' boundaries.

During the model design a COMSOL software user can specify the power of the heat source and the thermal conductivity of graphene. The temperature distribution in the flake is a result of the simulation runs. Thus any dependencies of the thermal conductivity can be studied only indirectly, since the thermal conductivity itself is the input for simulations. The simulation itself includes dividing (meshing) the modeled flake into an ensemble of flake's structural components and solving heat conduction equations for each component.

3.1. Model of Heat Propagation from a Hot Line Source

If the diameter of the laser sport is comparable to the width of the graphene flake, to simplify the solution one can approximate the shape of the heat source into an infinitesimally thin line, the length of which equals the width of the modeled flake. A graphene layer has a thickness of one carbon atom plane (~0.35 nm). Since it is rather thin, heating the top surface of the flake with the hot line can be seen as resulting in creating within the flake a uniformly hot surface normal to the flake's top or bottom surfaces.

The heated flake, which in COMSOL is called "the domain," is represented as a set of two identical subdomains, 1 and 2 (see Fig. 3). Each subdomain is a rectangular sheet with dimensions $W \times 2L \times h$. One subdomain is put into contact with another along one of its surfaces. This contact surface is a boundary with a heat flux directed inward normally to the sheet. The area of the contact surface is equal to Wh which is a product of the width of the sheet and its thickness. The boundary condition of the contact surface is specified using Fourier's law of heat conduction written in the form

$$\vec{n} \cdot (k \nabla T) = q_0 \tag{20}$$

where n is the magnitude of the unit vector normal to the contact surface of the subdomain and q_0 is the heat flux that enters the subdomain, [W/m^3].

In each subdomain the boundary that is opposite to the contact surface is specified as being kept at a constant prescribed temperature

$$T = T_0 \tag{21}$$

where $T_0 = 300$ K is the room temperature.

All other four subdomain's boundaries are defined as being completely insulated from the surrounding environment:

$$\vec{n} \cdot (k \nabla T) = 0 \tag{22}$$

i.e., the temperature gradient across the boundary is zero. This assumption simplifies the model but is reasonable. Graphene flake, besides being in contact with the heat sinks and being heated by the laser, can only interact with either air or silicon dioxide. Both air and silicon dioxide have thermal conductivities (0.024 Wm^{-1}K^{-1} and 1.28 W/m^{-1}K^{-1}, respectively) negligible if they are compared with the thermal conductivity of graphene, thus the heat propagation from graphene to either air or silicon dioxide can be ignored.

The heat propagation is modeled as two-dimensional. Due to the fact that the flake has just one atomic layer of arranged carbon atoms, and there are no interactions between graphene and air or silicon dioxide, the heat propagates entirely within the plane. In this model we can vary the power by assigning different values of the hot boundary heat flux (the cross-sectional area Wh is constant). Also, we can vary the thermal conductivity. The result of the simulation is a two-dimensional distribution of the temperature in the flake.

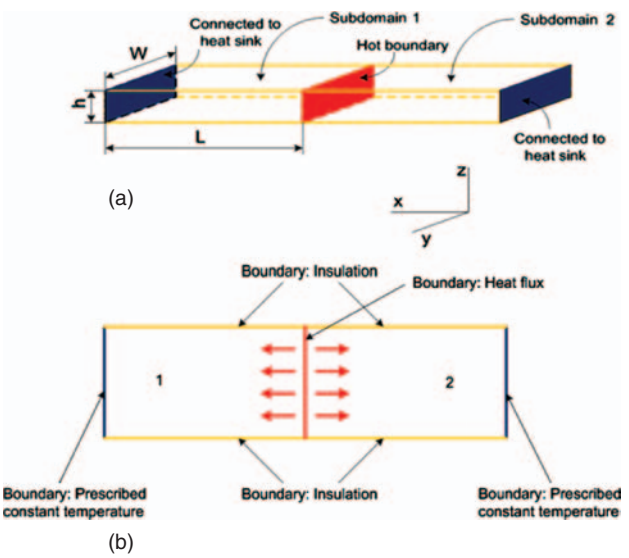

Fig. 3. Model of the flake heated by a hot line source: (a) Axonometric view; (b) View from top.

3.2. Model of Heat Propagation from a Hot Disk Source

During heating, the laser makes a sport on the graphene surface. The spot has a shape of a disk. The heat propagation in the graphene flake can be simulated considering this more realistic heat source. The areas within the laser spot are generally illuminated with different intensities. Also, there is no sharp edge between the spot and non-illuminated areas of the flake. Thus it is necessary to simulate the heat propagation with different radii of the spot to see how reduction of the size of the spot affects the heat conduction and whether the line source is indeed a good approximation for the laser spot. Since the flake is thin, heating the top plane of the flake with the hot disk

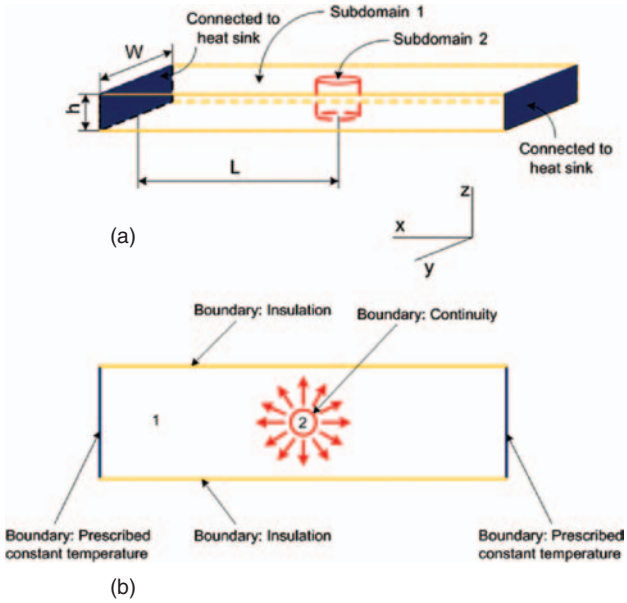

Fig. 4. Model of the flake heated by a disk source: (a) Axonometric view; (b) View from top.

can be seen as resulting in creating a uniformly hot cylinder embedded in the flake.

For the hot disk source model the flake is described as a set of two subdomains, 1 and 2 (see Fig. 4). Subdomain 1 is a parallelepiped with dimensions $W \times 2L \times h$. Subdomain 2 is a cylinder that is embedded in the parallelepiped and has a specific diameter. The height of the cylinder equals the thickness h of the parallelepiped. The axis of the cylinder is normal to the surface of the parallelepiped with sides W and $2L$ and passes through the geometrical center of the parallelepiped. The difference between this model and the model of the line heat source is that one of the subdomains, namely the subdomain 2, plays the role of a heat generator. In other words, the subdomain 2 contains a heat source within.

The heat conduction in this model is described by the heat equation derived from Fourier's law:

$$-\nabla \cdot (k\nabla T) = Q \tag{23}$$

where Q is the heat source, [W/m^3], which is defined as a heat energy generated within a unit volume per unit time.

The boundary between the subdomains 1 and 2, which is a "barrel" surface of the hot cylinder, is defined as a boundary with the continuous heat flux through it:

$$-\vec{n} \cdot (\vec{q}_1 - \vec{q}_2) = 0 \tag{24}$$

where n is the magnitude of the unit vector normal to the boundary between subdomains, q_1 is the magnitude of the flux of heat flowing out of the subdomain 1, and q_2 is the magnitude of the flux of heat flowing into the subdomain 2. The heat flux is normal to the "barrel" surface of the hot cylinder and is continuous across the boundary: the amount of the heat leaving the subdomain 2 per unit time per unit area equals the amount of the heat flowing into the subdomain 1 per unit time per unit area.

The opposite end surfaces of the subdomain 1 are connected to heat sinks. These boundaries of the subdomain 1 are prescribed to be kept at a constant temperature

$$T = T_0 \tag{25}$$

where $T_0 = 300$ K is the room temperature, like for the model of the line heat source.

All other four boundaries of the subdomain 1 and "end-cap" surfaces of the subdomain 2 are defined as being completely insulated from the surrounding environment:

$$\vec{n} \cdot (k\nabla T) = 0 \tag{26}$$

Like in the case of the line heat source, for the model of the hot disk source the heat propagation is assumed to be two-dimensional.

The heat source equals

$$Q = P/V \tag{27}$$

where P is the dissipated power and V is the volume of the subdomain 2.

We can vary the power P (the volume V of the subdomain 2 is constant) and the thermal conductivity. The result of the simulation is a two-dimensional distribution of the temperature in the flake.

3.3. Model of Heat Propagation from Gaussian Heat Source

The third considered heat source is Gaussian. It is interesting to investigate the case when the laser light intensity and the dissipated power follow the normal distribution. Due to a continuous nature of the Gaussian distribution, the heat source in this model cannot be isolated by boundaries. Neither the Gaussian source itself can be some boundary. Thus in this case, the flake is described as a single subdomain with a heat source within (see Fig. 5).

Like in the case for the disk source, the heat conduction in this model is described by the heat equation:

$$-\nabla \cdot (k\nabla T) = Q \tag{28}$$

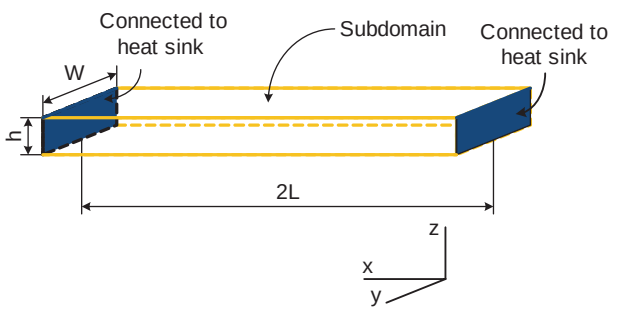

Fig. 5. Model of the flake heated by Gaussian heat source.

REVIEW

Here the heat source is defined as

$$Q = P/V \tag{29}$$

where V is the volume of the subdomain.

The dissipated power P follows the two-dimensional Gaussian distribution

$$P(X, Y) = P_{\text{peak}} \cdot e^{-((x^2/(2\sigma_x^2))+(y^2/(2\sigma_y^2)))} \tag{30}$$

where P_{peak} is the peak power. Sigmas can be varied but, for simplicity of the model, are assumed to be equal $\sigma = \sigma_x = \sigma_y$. The volume of the subdomain has a constant value. The Gaussian distribution reaches its peak at the geometrical center of the flake. Like in the case of the line or disk heat sources, the heat propagation is assumed to be two-dimensional, thus the dissipated power is a function of x and y coordinates, but not of z.

The opposite end surfaces of the subdomain are connected to heat sinks. These boundaries of the subdomain are modeled to be kept at a constant prescribed temperature

$$T = T_0 \tag{31}$$

where $T_0 = 300$ K is the room temperature, like for the models of the line and disk heat sources.

All other four boundaries of the subdomain are defined as being completely insulated from the surrounding environment:

$$\vec{n} \cdot (k \nabla T) = 0 \tag{32}$$

In this model the peak power P_{peak}, the sigma σ and the thermal conductivity can be varied. The result of the simulation is a two-dimensional distribution of the temperature in the flake.

4. EFFECTS OF A SHAPE OF A FLAKE: A LINE HEAT SOURCE

First simulation runs were dedicated to the studies how much the deviation of the shape from that of a parallelepiped (a rectangle if viewed from top) changes the heat conduction in the flake. We considered the line heat source. The following values were used as inputs for the simulation runs: (i) the power of the detector (spectrometer) P_{D}: 0.5 mW, 1.0 mW, 1.5 mW, 2.0 mW, and 2.7 mW, (ii) the thermal conductivity of graphene: 3000 $\text{Wm}^{-1}\text{K}^{-1}$, 3500 $\text{Wm}^{-1}\text{K}^{-1}$, 4000 $\text{Wm}^{-1}\text{K}^{-1}$, 4500 $\text{Wm}^{-1}\text{K}^{-1}$, 5000 $\text{Wm}^{-1}\text{K}^{-1}$, and 5500 $\text{Wm}^{-1}\text{K}^{-1}$.

Six shapes were analyzed. Figures 6–7 show views from top of each shape. Shape 1 viewed from top represents a rectangle with the length $L = 23$ μm and the width $W = 5$ μm. The excitation line from the heat source passes along the symmetry axis and divides the rectangle into two identical rectangles each with the length of 11.5 μm. Shape 2 viewed from top is a "butterfly"-type shape which is two identical isosceles trapezoids connected along their

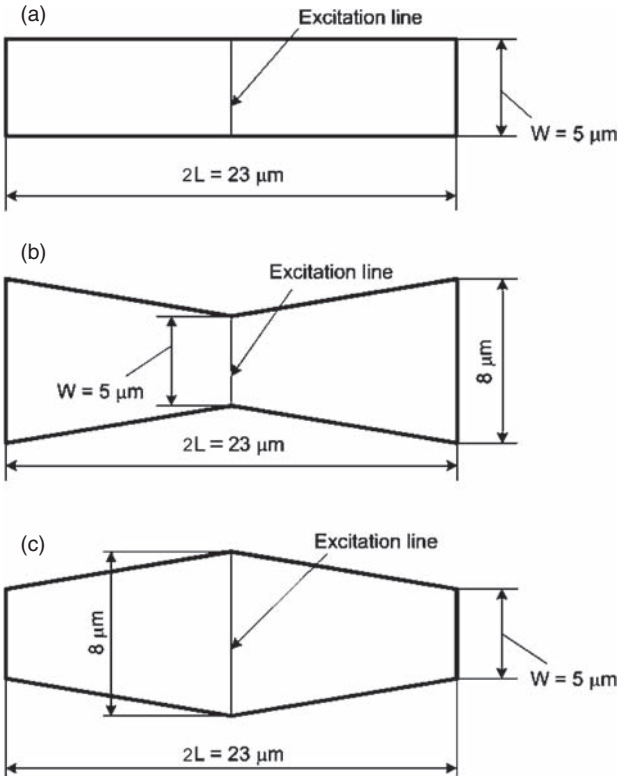

Fig. 6. (a) Shape 1, (b) Shape 2, (c) Shape 3.

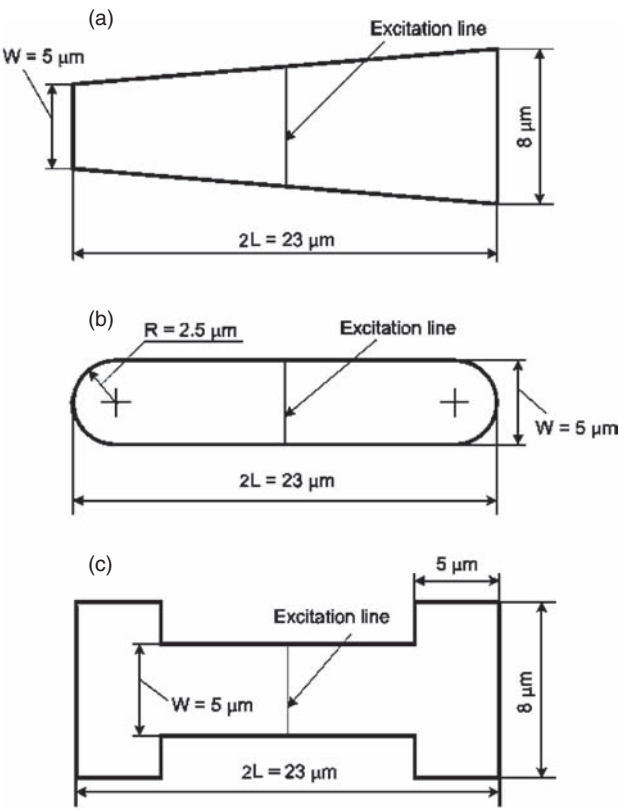

Fig. 7. (a) Shape 4, (b) Shape 5, (c) Shape 6.

small sides. The width of each trapezoid is $W = 5$ μm and the height is 11.5 μm. Shape 3 viewed from top is also a "butterfly"-type shape which is two identical isosceles trapezoids but connected along their large sides which have the widths of 8 μm. For both the Shape 2 and Shape 3 the excitation lines go along the connection lines. Shape 4 viewed from top is a trapezoid with the height $L = 23$ μm and widths $W = 5$ μm and 8 μm. The excitation line is parallel to both 5 μm and 8 μm sides and crosses the trapezoid at 11.5 μm from either 5 μm or 8 μm side. Shape 5 viewed from top represents a rectangle with the width $W = 5$ μm and the length 18 μm connected at its small sides to two half-disks. The radius of each half-disk is equal to 2.5 μm. The excitation line is perpendicular to both straight lines of the rectangle and passes at 9 μm from either of two small sides of the rectangle. Shape 6 viewed from top is "H"-type shape made of three rectangles. One rectangle has the width $W = 5$ μm and the length of 13 μm. Two identical rectangles with the widths of 5 μm and the lengths of 8 μm are connected to the large rectangle in such a way that the large line of symmetry of the 5 μm $\times$ 13 μm rectangle coincides with the small lines of symmetry of the 5 μm $\times$ 8 μm rectangles.

By varying the input power and thermal conductivity we were able to extract a temperature profile for each shape. Simulated temperature profiles are shown in Figures 8–9. The linearity of the heat source defines the linear front of the heat wave. Subsequently, linear temperature drop was observed in the Shape 1 flake from the excitation line to the surfaces connected to the heat sinks. It was found that only the Shape 6 mostly preserves the linearity of the temperature drop along the flake. Rounded ends of the Shape 5 result in non-linear behavior of the temperature. Also, in the Shapes 2, 3 and 4 the temperature decreases non-linearly from the excitation line to the ends. This is due to a constant change in the width of the flake; the width is not equal to the length of the excitation line everywhere but exactly at the excitation line. The plane heat front gets disturbed in the Shapes 2, 3 and 4, because the cross-section of the flake changes along the large symmetry axis, thus the area, through which the heat flows, changes from its original value (measured under the excitation line).

By studying a temperature profile for each shape one can analyze how the temperature at the excitation line (the maximum temperature) depends on the power of the

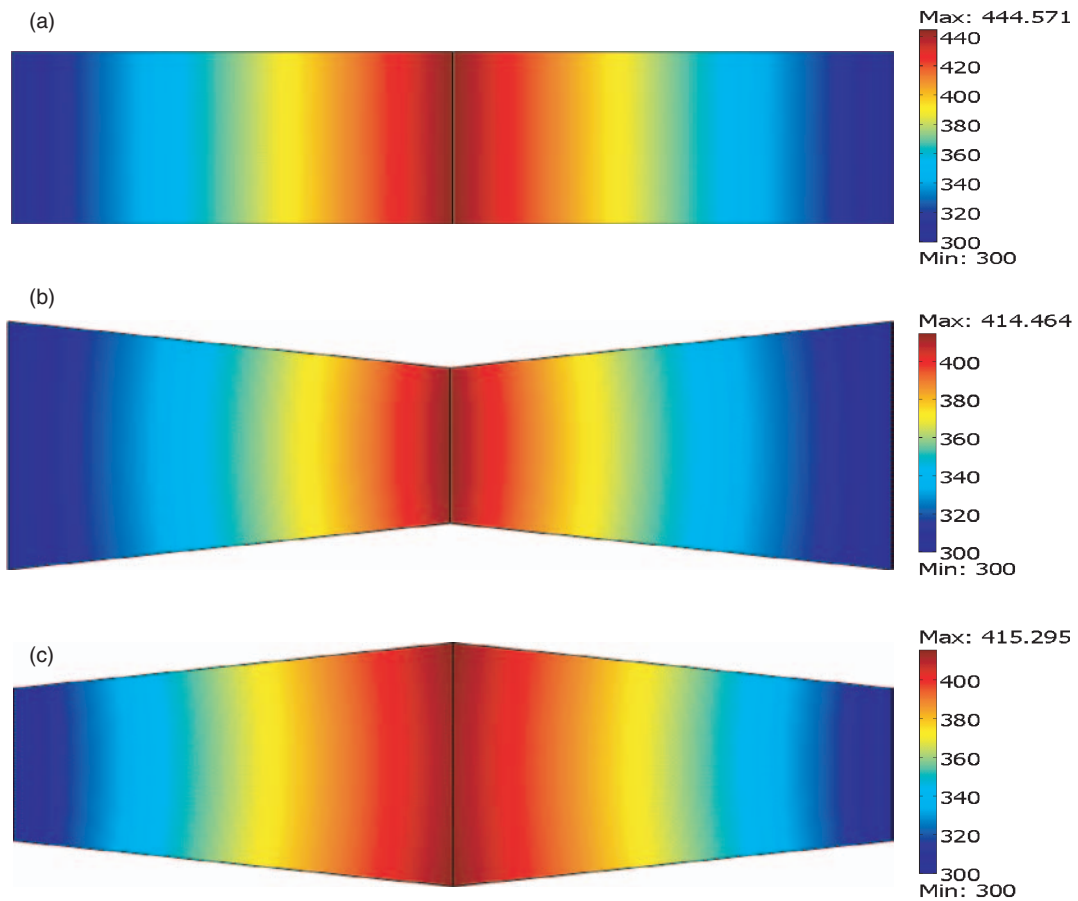

Fig. 8. Temperature profile of the flake heated with the line source: (a) Shape 1, (b) Shape 2, (c) Shape 3. The excitation power is $P_D = 2$ mW and the thermal conductivity is $k = 5000$ $Wm^{-1}K^{-1}$.

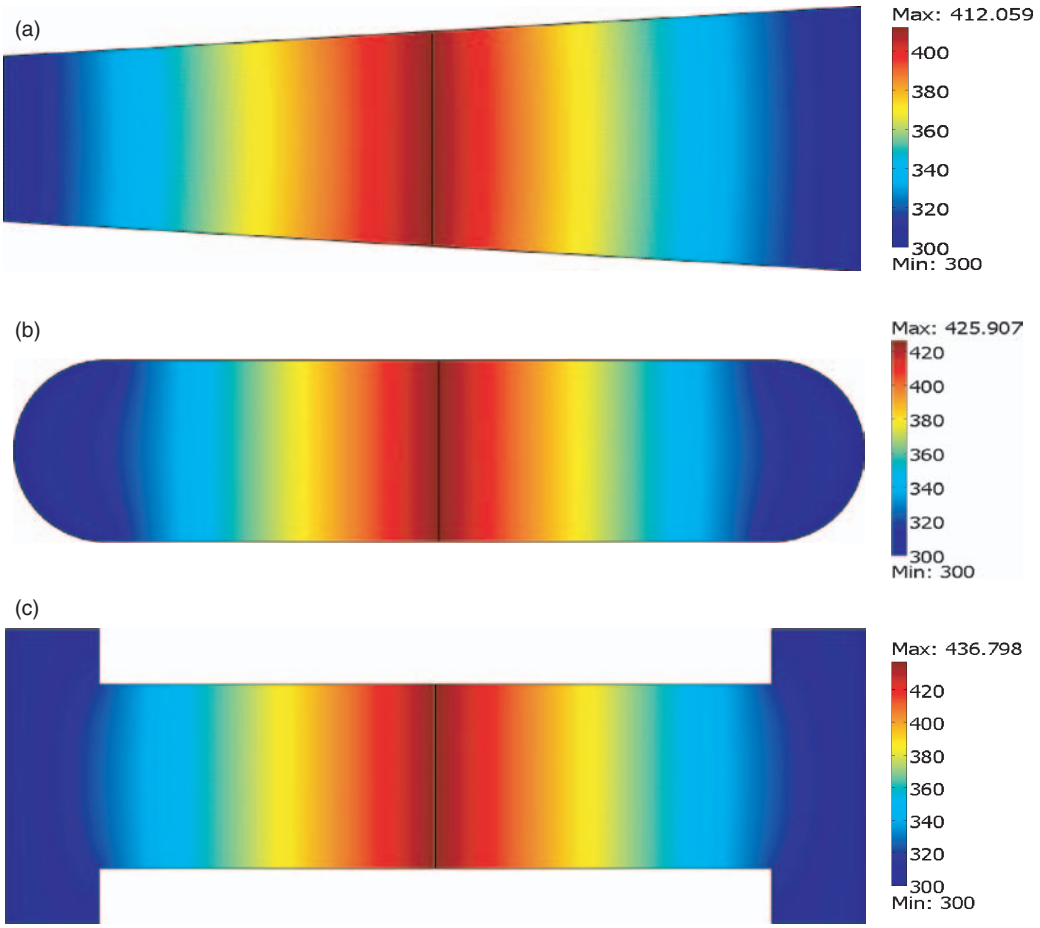

Fig. 9. Temperature profile of the flake heated with the line source: (a) Shape 4, (b) Shape 5, (c) Shape 6. The excitation power is $P_D = 2$ mW and the thermal conductivity is $k = 5000$ $Wm^{-1}K^{-1}$.

detector for each studied shape. Figure 10 plots such functions. From the analysis of those plots we can conclude that

(1) higher thermal conductivity of graphene results in lower maximum temperature,

(2) when the power of the detector is small (0.5 mW) the maximum temperature is approximately same for all shapes,

(3) an increase in the power of the detector corresponds to an increase of the maximum temperature; such increase of the temperature is more pronounced for flakes with lower thermal conductivities.

We can also compare different shapes by analyzing their maximum temperatures for certain thermal conductivities. Figure 11 shows such analysis for flakes with the thermal conductivities $k = 3500$ $Wm^{-1}K^{-1}$ and $k = 5000$ $Wm^{-1}K^{-1}$. For both cases, the highest temperatures at the excitation lines are reached when the flakes have geometries of the Shape 1, i.e., rectangular (viewed from top) shapes. Second to the highest value of the temperature is observed for the Shape 6. The lowest temperatures correspond to the "butterfly" Shapes 2 and 3 and the trapezoid Shape 4.

The thermal conductivity of single layer graphene was measured as

$$k = \left(\frac{\eta L}{2Wh}\right) \cdot \chi\theta^{-1} = \left(\frac{\eta L}{2\beta Wh}\right) \cdot \left(\frac{\delta\omega}{\delta T}\right) \cdot \left(\frac{\delta P}{\delta\omega}\right) \quad (33)$$

taking in consideration that the flake had a parallelepiped (rectangular if viewed from top) shape and the heat was transferring from a line laser source. The measurements were done without actually measuring the temperature at the excitation line, and both coefficients

$$\chi = \delta\omega/\delta T = 0.016 \text{ cm}^{-1}\text{K}^{-1} \quad (34)$$

and

$$\theta = \delta\omega/\delta P = 1.226 \text{ cm}^{-1}(\text{mW})^{-1} \quad (35)$$

were set to be constant.

In simulations both the power and thermal conductivity are input parameters, and the temperature at the excitation line has to be computed. We can study the function

$$k = f(\theta^{-1}) \quad (36)$$

where

$$\theta^{-1} = \left(\frac{\delta P}{\delta\omega}\right) = \left(\frac{\delta P}{\chi\delta T}\right) \quad (37)$$

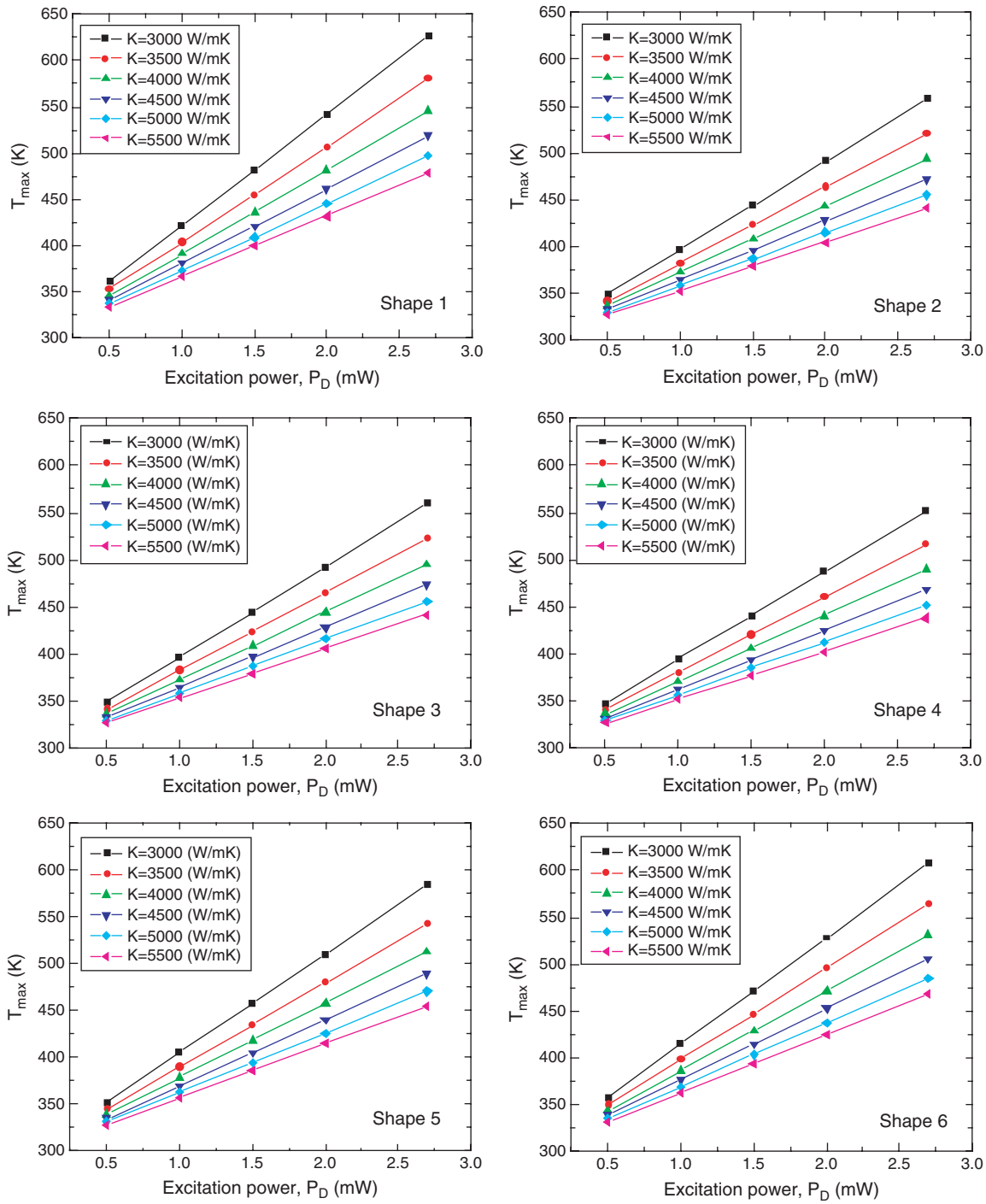

Fig. 10. Temperature at the center of the excitation line as a function of the detector power for different values of graphene's thermal conductivity and different shapes.

assuming that the temperature coefficient χ remains constant. The example of the simulated $k = f(\theta^{-1})$ spectrum for the Shape 1 is shown in Figure 12. Such spectrum gives an insight how a shape irregularity from a perfect rectangular form and an actual difference of the heat source from a line affect the measured thermal conductivity. In the experiments both functions of the G peak position versus the temperature and the G peak position versus the power were independent from the shapes of the flake and source. The shapes of the flake and source were taken into consideration when the thermal conductivity was derived. We can do an opposite task and use simulation results, together with the calculated spectrum $k = f(\theta^{-1})$, to find an expected value of the thermal conductivity for each type

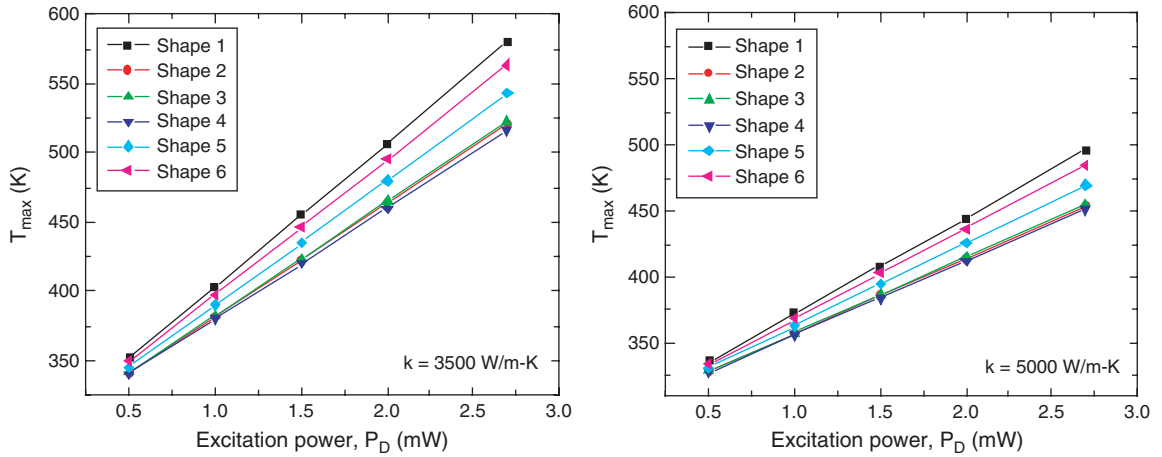

Fig. 11. Maximum temperatures in the graphene flake for different shapes when the thermal conductivity is equal to $k = 3500$ $\mathrm{Wm^{-1}K^{-1}}$ or $k = 5000$ $\mathrm{Wm^{-1}K^{-1}}$.

of shapes and sources. For example, referring to Figure 12, having $k = f(\theta^{-1})$ spectrum, we can choose the point $\theta = 1.226$ $\mathrm{cm^{-1}(mW)^{-1}}$ and find the expected value of the thermal conductivity for the parallelepiped shape to be $k = 4766$ $\mathrm{Wm^{-1}K^{-1}}$.

Table I summarizes the simulation results of the heat conduction through the flakes of different shapes when the line source is used.

The table compares the surface areas of all shapes, the temperatures at the excitation lines (T_{max}) when the power of the detector equals 2 mW, and when the simulated thermal conductivity of the flake equals 5000 $\mathrm{Wm^{-1}K^{-1}}$. Also, the expected thermal conductivities for different flakes are compared for a chosen parameter $\theta = 1.226$ $\mathrm{cm^{-1}(mW)^{-1}}$. From the presented data we can conclude that the heat conduction in the Shape 6 flake resembles the heat conduction in the Shape 1 flake. Both the maximum temperature and expected thermal conductivity for the Shape 6 are

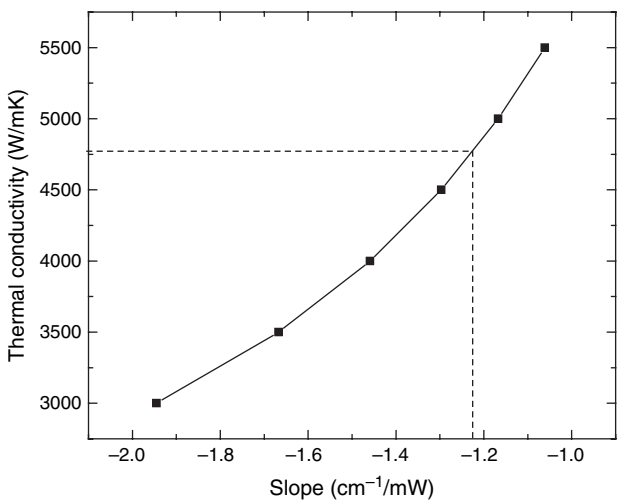

Fig. 12. Thermal conductivity of the parallelepiped graphene flake as a function of the parameter $\theta = \delta\omega/\delta P$ (slope) when the line laser source is used.

similar to those that correspond to the Shape 1. We might speculate that for the line source, when the heat waves form a plane front within the flake, the nature of the heat propagation is defined by the ratio of the flake's width to the flake's length and rectangularity of the flake. Viewing both the Shape 1 and Shape 6 from top, each of these shapes is essentially rectangular for a substantial distance from the excitation line, and the width of the rectangle is small compared to the length of the rectangle. Only at the "ends" of the rectangle, the Shape 1 is "modified" into the Shape 6 by increasing the width of the rectangle. Since those enlarged ends are connected to the heat sinks which are kept under an ambient temperature, the picture of the heat propagation is not changed much, thus the expected thermal conductivity and temperature at the excitation line are almost the same as for the case of an "unmodified" rectangle. Partially the above mentioned argument is supported by the fact that the Shape 5 also shows the maximum temperature and expected thermal conductivity to be close to those of the Shape 1. They are lower than for either the Shape 1 or the Shape 6, because the total area of the flake is reduced. Moreover, the width of the Shape 5 flake reduces fast at the ends of the flake, thus reducing the surface of the heat front that approaches the heat sinks.

We can argue that both the Shape 5 and Shape 6 viewed from top to some extent resemble the rectangular shapes in areas of the flake which are near the excitation line, thus such flakes display the thermal characteristics similar to those of the "perfect" Shape 1 parallelepiped. The Shapes 2, 3, and 4 represent opposite phenomena when the shapes viewed from top are substantially different from a rectangle, particularly in the area near the excitation line. In our specific example, the areas of the Shapes 2, 3, and 4 are larger by 1.6 compared to that of the Shape 1. But both the maximum temperature and expected thermal conductivity are lower (the temperature is approximately 93% and the expected thermal conductivity is approximately 80%

Table I. Effects of different geometries on the temperature and expected thermal conductivity when the line source is applied. Both the length L and minimum width W of the flake are kept constant. A is the surface area of the flake; A_0 is the surface area of the Shape 1 flake; T_{max} is the maximum temperature when the excitation power is $P_D = 2$ mW and the thermal conductivity of graphene is $k = 5000$ $Wm^{-1}K^{-1}$; T_{0_max} is the maximum temperature when the excitation power is $P_D = 2$ mW, the thermal conductivity of graphene is $k = 5000$ $Wm^{-1}K^{-1}$, and the flake has Shape 1 geometry; k is the expected thermal conductivity of graphene when $\theta = 1.226$ $cm^{-1}(mW)^{-1}$; k_0 is the expected thermal conductivity of graphene when $\theta = 1.226$ $cm^{-1}(mW)^{-1}$ and the flake has Shape 1 geometry.

Geometry	A (m^2)	A/A_0 (%)	T_{max} (K)	T_{max}/T_{0_max} (%)	k ($Wm^{-1}K^{-1}$)	k/k_0 (%)
Shape 1	1.15×10^{-10}	100	444.57	100	4766.20	100
Shape 2	1.84×10^{-10}	160.87	414.46	93.23	3758.53	78.86
Shape 3	1.84×10^{-10}	160.87	415.30	93.42	3782.40	79.36
Shape 4	1.84×10^{-10}	160.87	412.06	92.69	3676.68	77.14
Shape 5	1.10×10^{-10}	95.65	425.91	95.80	4124.25	86.53
Shape 6	1.30×10^{-10}	113.04	436.80	98.25	4477.20	93.94

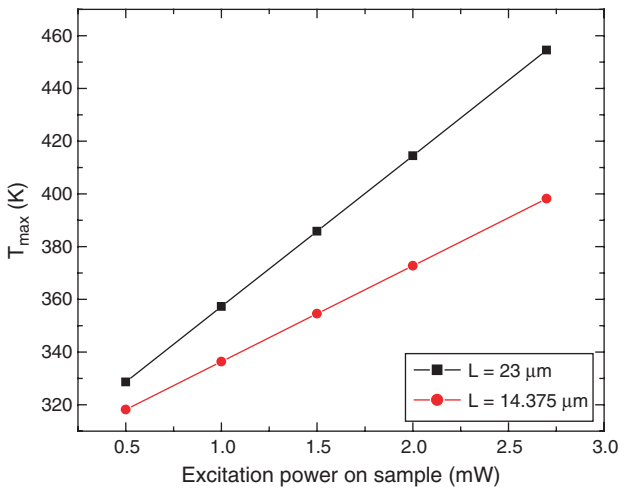

Fig. 13. Maximum temperature as a function of the detector power in Shape 2 when either the length or the surface area matches that of the Shape 1. The thermal conductivity is 5000 $Wm^{-1}K^{-1}$.

of the temperature and expected thermal conductivity, correspondingly, of the Shape 1 flake). An increase of the flake's width (in average, and in some areas), and a constant change of the width along the large symmetry axis produce such an effect.

The described simulations were done considering all shapes having the same lengths L and minimum widths W. Thus the surface areas of the flakes were different for different shapes. We also performed similar studies, considering all shapes having the same surface areas and minimum widths W. For such simulation runs we varied the length L to adjust the surface area of any particular shape to that of the Shape 1. Figure 13 shows an example of the simulated maximum temperature as a function of the detector power for the flake that has the Shape 2 type, and which thermal conductivity is 5000 $Wm^{-1}K^{-1}$. With the reduced L the temperature rises with the power not as fast as in the case of the original dimension $L = 23$ μm.

Table II summarizes the simulations of the heat conduction through the flakes of different shapes when the line source is used and when the surface areas and the minimum widths are fixed.

Only the flake of the Shape 5 has the length increased by 1.05 if compared with the Shape 1 parallelepiped. For all shapes both the maximum temperature and expected thermal conductivity are dropped. But such drop is minimal for the Shape 5, largely because the length is increased. The flakes that have geometries of the Shapes 2, 3, 4, and 6 have their lengths reduced to 63–65% of the original 23 μm. The Shape 6 does not show significant reductions in the temperature and expected thermal conductivity due to rectangularity of this shape and still a small fraction W/L. However, the expected thermal conductivity drops as much as twice in the "butterfly" and trapezoid flakes (the maximum temperatures are 83–84% of the maximum temperature in the Shape 1 flake).

Table II. Effects of different geometries on the temperature and expected thermal conductivity when the line source is applied. Both the surface area and minimum width W of the flake are kept constant. L is the length of the flake; L_0 is the length of the Shape 1 flake; T_{max} is the maximum temperature when the excitation power is $P_D = 2$ mW and the thermal conductivity of graphene is $k = 5000$ $Wm^{-1}K^{-1}$; T_{0_max} is the maximum temperature when the excitation power is $P_D = 2$ mW, the thermal conductivity of graphene is $k = 5000$ $Wm^{-1}K^{-1}$ and the flake has Shape 1 geometry; k is the expected thermal conductivity of graphene when $\theta = 1.226$ $cm^{-1}(mW)^{-1}$; k_0 is the expected thermal conductivity of graphene when $\theta = 1.226$ $cm^{-1}(mW)^{-1}$ and the flake has Shape 1 geometry.

Geometry	L (μm)	L/L_0 (%)	T_{max} (K)	T_{max}/T_{0_max} (%)	k ($W/m^{-1}K^{-1}$)	k/k_0 (%)
Shape 1	23.000	100	444.57	100	4766.20	100
Shape 2	14.375	62.50	372.74	83.84	2386.44	50.07
Shape 3	14.375	62.50	374.21	84.17	2429.93	50.98
Shape 4	14.375	62.50	369.92	83.21	2314.81	48.57
Shape 5	24.072	104.66	431.70	97.11	4319.07	90.62
Shape 6	15.000	65.22	418.17	94.06	3870.72	81.21

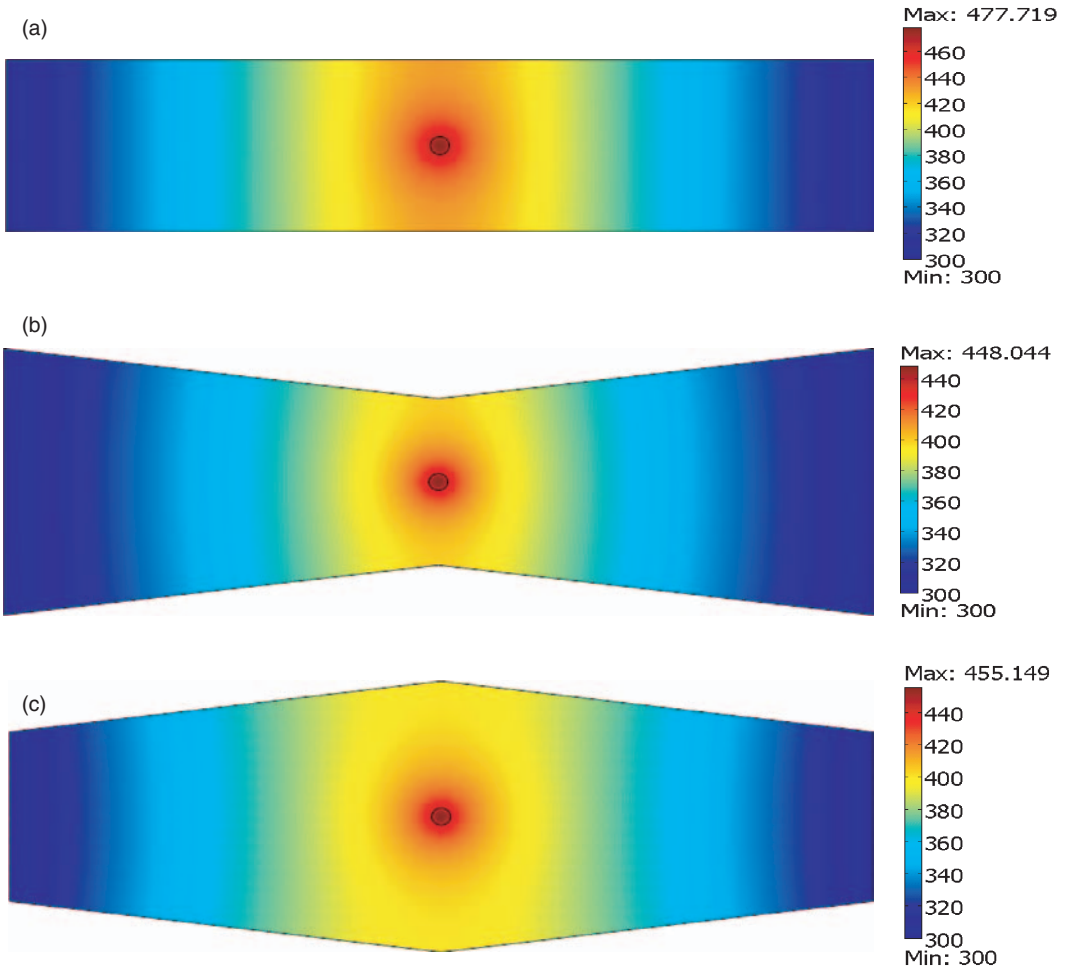

Fig. 14. Temperature profile of the flake heated with the disk source: (a) Shape 1, (b) Shape 2, (c) Shape 3. The excitation power is $P_D = 2$ mW and the thermal conductivity is $k = 5000$ $Wm^{-1}K^{-1}$. The diameter of the laser spot is 0.5 μm.

5. EFFECTS OF A SHAPE OF A FLAKE: A DISK HEAT SOURCE

During the measurement of the thermal conductivity of graphene, the heat source was approximated to be the line source. It is interesting to investigate how good such an approximation was. In simulations we replaced the line heat source with a disk heat source. The diameter of the heated disk is taken as 0.5 μm which is close to the diameter of the laser spot during the experiment. We considered the same six shapes of the flake and run simulations again varying the detector power from 0.5 to 2.7 mW and the thermal conductivity from 3000 to 5500 $Wm^{-1}K^{-1}$. As a result, temperature profiles and functions T_{max} versus P_D were extracted for each shape and the assigned value of the thermal conductivity.

Figures 14–15 present the temperature profiles for each shape when the heat source has disk geometry. Figure 16 shows the maximum temperatures as functions of the detector power for particular values of the thermal conductivity. Inspection of the plots in Figure 16 allows us to state that the increase of the temperature, as the detector power increases, shows the trends very similar to those observed in the cases of the line sources. But, when the disk heat source is used, the maximum temperature rises faster, as the power increases.

Table III summarizes the simulations of the heat conduction through the flakes of different shapes when the disk heat source is used. The detector power is assumed to be 2 mW and the thermal conductivity of the flake is assigned to be 5000 $Wm^{-1}K^{-1}$. The flakes of different shapes have different surface areas, but the same lengths and minimum widths. If compared with the data in Table I, these results show that, when the hot disk source is used, the geometry of the flake influences changes in the maximum temperature in a very similar way, as when the heat source is a line. But the "butterfly" and trapezoid geometries of the Shapes 2, 3 and 4 have lesser effects on the expected thermal conductivity compared to the situation with the line source.

As in the case of the line source, the heat conduction in the Shape 6 flake most closely resembles the heat conduction in the parallelepiped Shape 1 flake.

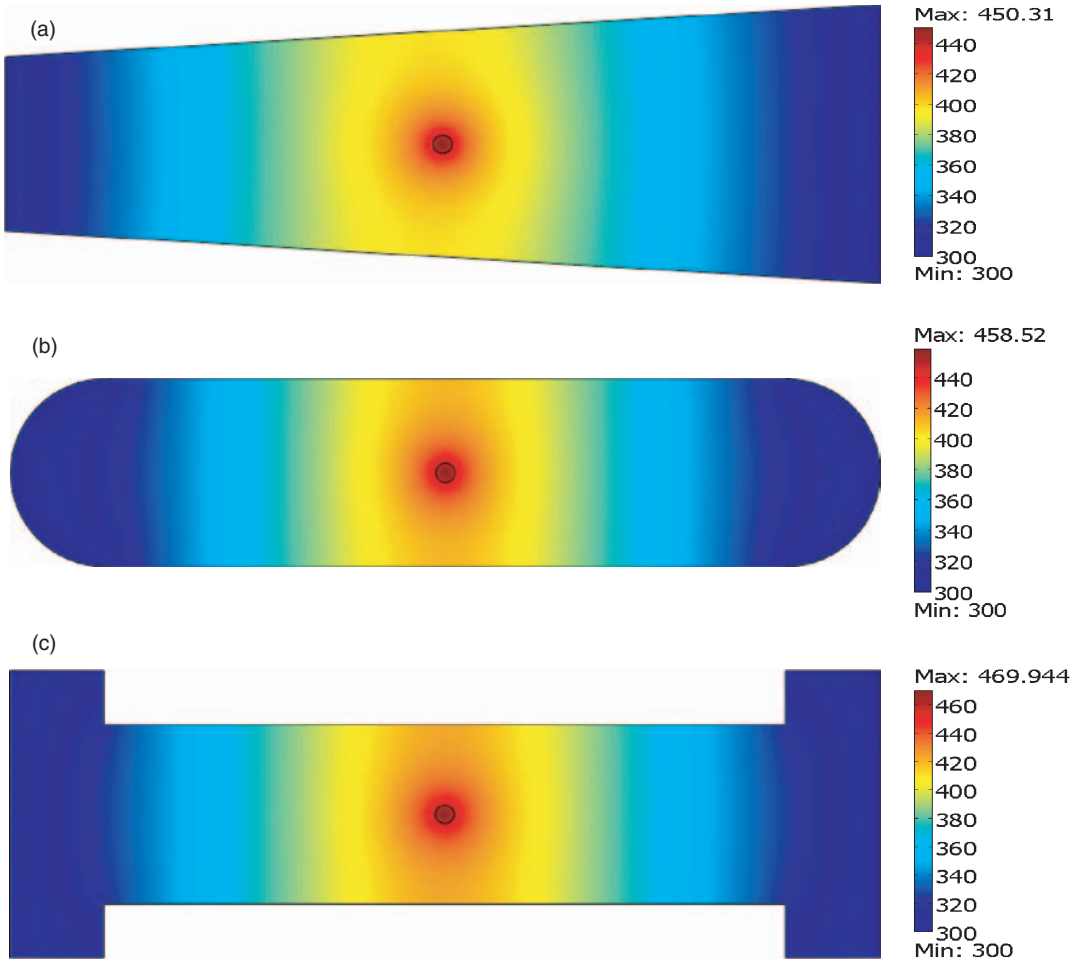

Fig. 15. Temperature profile of the flake heated with the disk source: (a) Shape 4, (b) Shape 5, (c) Shape 6. The excitation power is $P_D = 2$ mW and the thermal conductivity is $k = 5000$ $Wm^{-1}K^{-1}$. The diameter of the laser spot is 0.5 μm.

6. EFFECTS OF A GEOMETRY OF A SOURCE: A DISK AND GAUSSIAN HEAT SOURCES

It is interesting to see how the geometry of the heat spot affects the simulated heat conduction. To investigate this we can directly compare the heat conduction profiles for the line and the disk sources, vary the sizes of the disk spots or replace the disk laser spot with Gaussian heat source.

Table IV provides a direct reference-comparison of the maximum temperatures and expected thermal conductivities for different shapes ($P_D = 2$ mW and $k = 5000$ $Wm^{-1}K^{-1}$). As it was mentioned, the maximum temperature slightly drops in all shapes when the geometry changes from a perfect parallelepiped. The percentage of the drop in the temperature in the case of the line heat source is almost identical to the percentage of such drop when the hot disk source is used. However, with the disk source the expected thermal conductivity is less dependent on the shapes than when the heat source is a line. Obviously, variation of the shape from a parallelepiped has a stronger effect when the heat waves travel in a line (plane) front. When the heat travels along the longer side of the flake, the propagation of the front is affected by how the width of the flake changes. But, when the source has disk geometry, the heat waves form a circular front, thus, at least in the areas near the source, the heat propagates independently of the shape of the flake. The data in the table supports the fact that in the cases of the line source and the "butterfly" or trapezoid shapes the heat propagation is strongly affected by the geometry of the flake.

Table V directly compares the maximum temperatures and the expected thermal conductivities extracted under the same conditions ($P_D = 2$ mW and $k = 5000$ $Wm^{-1}K^{-1}$) for the line and the disk heat sources. The very fact that the heat source has a disk shape results in increases in both the temperature and thermal conductivity. The temperature is increased by 7–10% and the thermal conductivity is increased by 22–34% when we change the model of the heat source from the line to the disk. It is interesting to see that the flakes that resemble parallelepipeds better (the Shapes 5 and 6) show less dependence on the geometry of the source. This effect is especially seen in the values of the expected thermal conductivity. While the disk

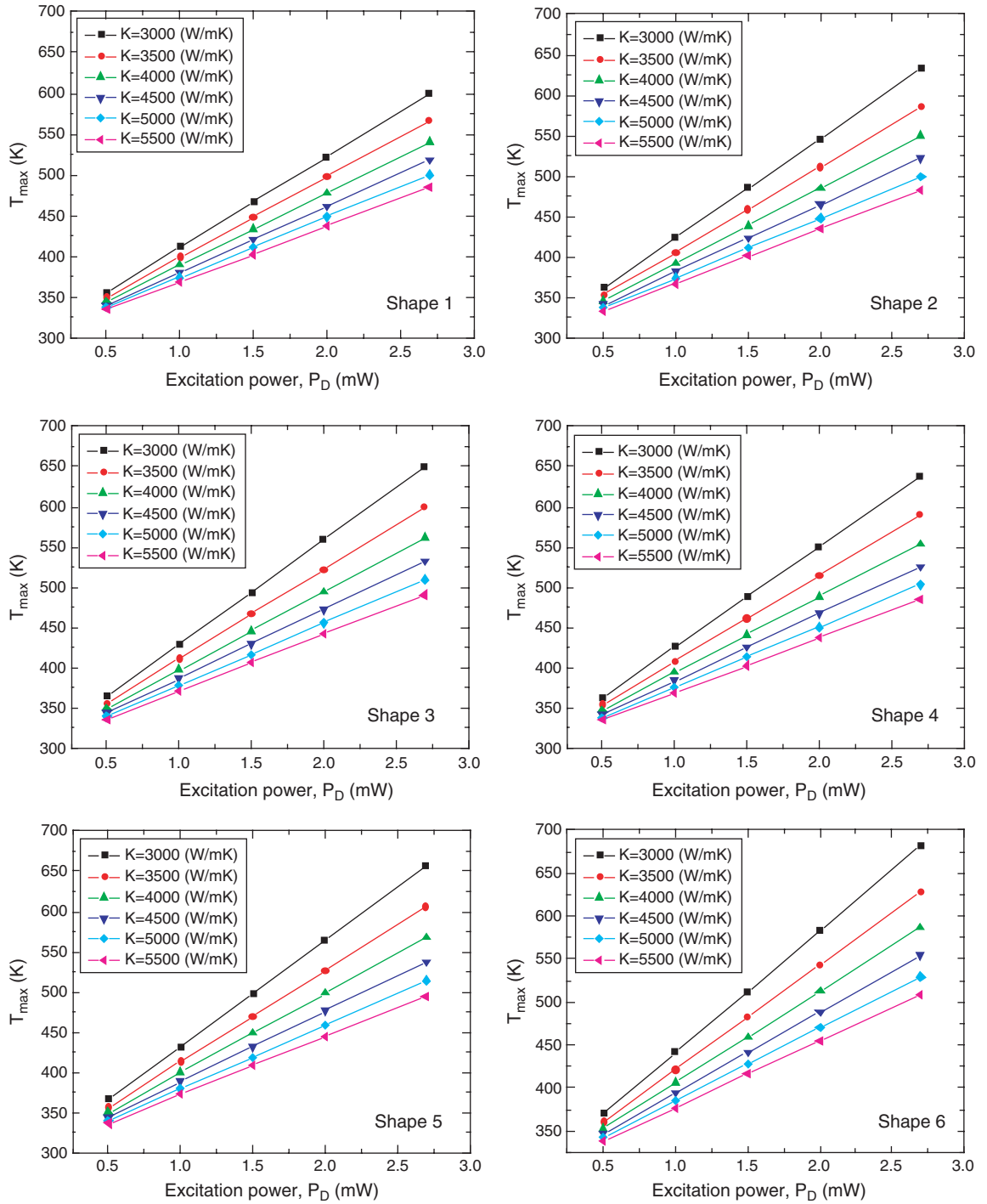

Fig. 16. Temperature at the center of the laser spot (disk source) as a function of the detector power for different values of graphene's thermal conductivity and different shapes.

heat source models for the Shapes 5 and 6 show 25–26% increases compared to the line source models, the expected thermal conductivity is increased by 29–34% in the "butterfly" and trapezoid flakes. The difference between the line and the disk heat sources is not so obvious if the flake resembles a parallelepiped and when the width W is small compared to the length L.

According to Table V, the expected thermal conductivities of the rectangular Shape 1 and the H-type Shape 6 are both higher than the thermal conductivity reported by the experiment. If during the experiment the dimensions of the flake were evaluated correctly, approximation of the disk source by the line source results in underestimation of the thermal conductivity during calculations. Moreover, such

Table III. Effects of different geometries on the temperature and expected thermal conductivity when the disk heat source is used. Both the length L and minimum width W of the flake are kept constant. A is the surface area of the flake; A_0 is the surface area of the Shape 1 flake; T_{max} is the maximum temperature when the excitation power is $P_D = 2$ mW and the thermal conductivity of graphene is $k = 5000$ $Wm^{-1}K^{-1}$; T_{0_max} is the maximum temperature when the excitation power is $P_D = 2$ mW, the thermal conductivity of graphene is $k = 5000$ $Wm^{-1}K^{-1}$ and the flake has Shape 1 geometry; k is the expected thermal conductivity of graphene when $\theta = 1.226$ $cm^{-1}(mW)^{-1}$; k_0 is the expected thermal conductivity of graphene when $\theta = 1.226$ $cm^{-1}(mW)^{-1}$ and the flake has Shape 1 geometry.

Geometry	A (m^2)	A/A_0 (%)	T_{max} (K)	T_{max}/T_{0_max} (%)	k ($Wm^{-1}K^{-1}$)	k/k_0 (%)
Shape 1	1.15×10^{-10}	100	477.72	100	5816.80	100
Shape 2	1.84×10^{-10}	160.87	447.99	93.78	4843.52	83.27
Shape 3	1.84×10^{-10}	160.87	455.15	95.28	5067.79	87.12
Shape 4	1.84×10^{-10}	160.87	450.31	94.26	4914.30	84.48
Shape 5	1.10×10^{-10}	95.65	458.52	95.98	5185.47	89.15
Shape 6	1.30×10^{-10}	113.04	469.94	98.37	5578.88	95.91

Table IV. Maximum temperatures and expected thermal conductivities for the cases of the line and disk heat sources. T_{max} is the maximum temperature when the excitation power is $P_D = 2$ mW and the thermal conductivity of graphene is $k = 5000$ $Wm^{-1}K^{-1}$; T_{0_max} is the maximum temperature when the excitation power is $P_D = 2$ mW, the thermal conductivity of graphene is $k = 5000$ $Wm^{-1}K^{-1}$ and the flake has Shape 1 geometry; k is the expected thermal conductivity of graphene when $\theta = 1.226$ $cm^{-1}(mW)^{-1}$; k_0 is the expected thermal conductivity of graphene when $\theta = 1.226$ $cm^{-1}(mW)^{-1}$ and the flake has Shape 1 geometry.

Geometry	T_{max}/T_{0_max} (%), line source	T_{max}/T_{0_max} (%), disk source	k/k_0 (%), line source	k/k_0 (%), disk source
Shape 1	100	100	100	100
Shape 2	93.23	93.78	78.86	83.27
Shape 3	93.42	95.28	79.36	87.12
Shape 4	92.69	94.26	77.14	84.48
Shape 5	95.80	95.98	86.53	89.15
Shape 6	98.25	98.37	93.94	95.91

a simulation result hints that the true value of the single layer graphene thermal conductivity is closer to its upper reported bound (5300 $Wm^{-1}K^{-1}$) rather than to its lower bound (3080 $Wm^{-1}K^{-1}$).

We can also investigate how the sizes of the laser spots affect the simulated temperature and expected thermal conductivity. Figure 17 presents the temperature profiles for the Shape 1 flakes when the heat sources are disks and the diameters of the disks are 0.005 μm, 0.05 μm and 5 μm. The local temperatures as functions of the coordinates along the large symmetry axis of the Shape 1 are shown in Figure 18 for the 0.05 μm and in Figure 19 for the 5 μm disk sources. Both plots suggest that this function is highly non-linear in the areas close to the center of the laser spot, but linearizes as the distance from the center of the spot increases. Figure 20 shows the maximum temperatures as functions of the detector power for chosen values of the thermal conductivity. The temperature increases very rapidly with the power in cases of small laser spots, 0.005 μm and 0.05 μm.

Table VI illustrates the results of the simulated maximum temperature ($P_D = 2$ mW and $k = 5000$ $Wm^{-1}K^{-1}$) and expected thermal conductivity for different disk diameters. The Shape 1 was considered. It is seen that the reduction of the size of the spot leads to an increased maximum temperature and an increased expected thermal conductivity, but such increases are functionally weaker compared to the size modification. Reducing the size by a factor of 10 results in just 10% increase in the temperature and 26% increase in the expected thermal conductivity. Reducing the size by a factor of 100 leads to 18% increase in the temperature and 50% increase in the thermal conductivity. Increase of the size of the spot by 100 makes the temperature drop by 10% and the thermal conductivity drop by 26%.

According to the table the expected thermal conductivities for the 0.05 μm and 0.005 μm laser spots are unrealistically high. We might conclude that it is unlikely that the laser spots can be modeled as the spots with such small diameters. The model of the 5 μm spot shows the expected thermal conductivity to be within the range reported by

Table V. Direct comparison of the maximum temperatures and expected thermal conductivities for the cases of the line and disk heat sources. T_{max_line} is the maximum temperature when the excitation power is $P_D = 2$ mW, the thermal conductivity of graphene is $k = 5000$ $Wm^{-1}K^{-1}$ and the line heat source is used; T_{max_disk} is the maximum temperature when the excitation power is $P_D = 2$ mW, the thermal conductivity of graphene is $k = 5000$ $Wm^{-1}K^{-1}$ and the disk heat source is used; $k_{\_line}$ is the expected thermal conductivity of graphene when $\theta = 1.226$ $cm^{-1}(mW)^{-1}$ and the line heat source is used; $k_{\_disk}$ is the expected thermal conductivity of graphene when $\theta = 1.226$ $cm^{-1}(mW)^{-1}$ and the disk heat source is used.

Geometry	T_{max_line} (K)	T_{max_disk} (K)	$T_{max\_disk}/T_{max\_line}$ (%)	$k_{\_line}$ ($Wm^{-1}K^{-1}$)	$k_{\_disk}$ ($Wm^{-1}K^{-1}$)	$k_{\_disk}/k_{\_line}$ (%)
Shape 1	444.57	477.72	107.47	4766.20	5816.80	122.04
Shape 2	414.46	447.99	108.09	3758.53	4843.52	128.87
Shape 3	415.30	455.15	109.60	3782.40	5067.79	133.98
Shape 4	412.06	450.31	109.28	3676.68	4914.30	133.66
Shape 5	425.91	458.52	107.66	4124.25	5185.47	125.73
Shape 6	436.80	469.94	107.59	4477.20	5578.88	124.61

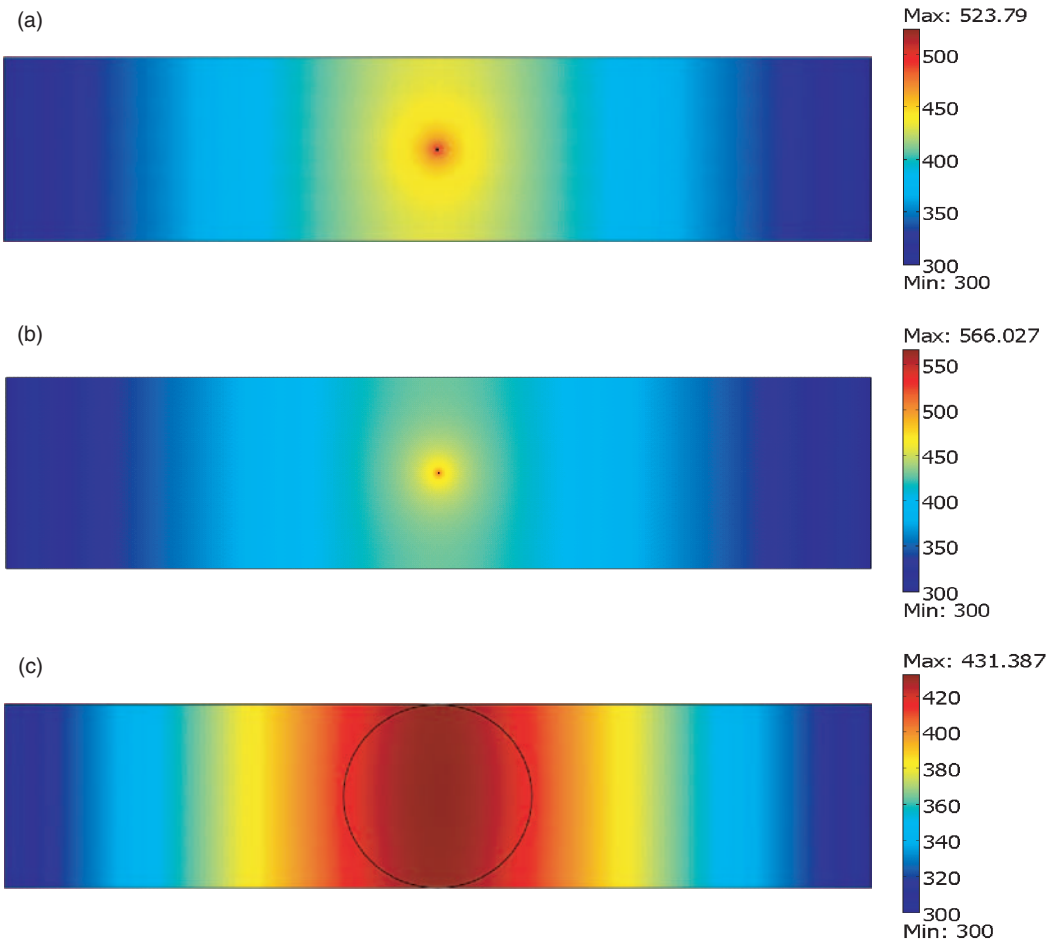

Fig. 17. Temperature profile of the flake heated with the disk source. The excitation power is $P_D = 2$ mW and the thermal conductivity is $k = 5000$ $Wm^{-1}K^{-1}$. The diameter of the laser spot is (a) 0.05 μm, (b) 0.005 μm, and (c) 5 μm.

the experiment. Thus the large disk spot is not in contradiction with observations. Also, since the diameter of such a big spot equals the width of the flake, the front of the propagating heat in the flake will be predominantly linear, thus the 5 μm disk source can surely be approximated as a line heat source.

It is not clear what kind of distribution the laser beam follows. We investigated whether the model of the heat

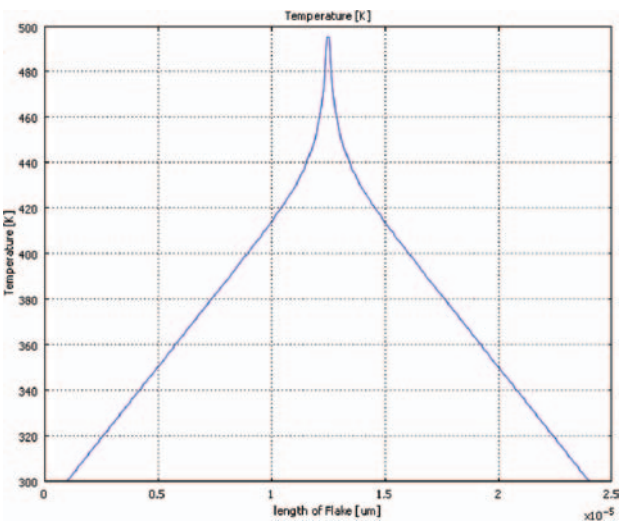

Fig. 18. Local temperature as a function of the coordinate along the large symmetry axis. Disk heat source with a diameter of 0.05 μm.

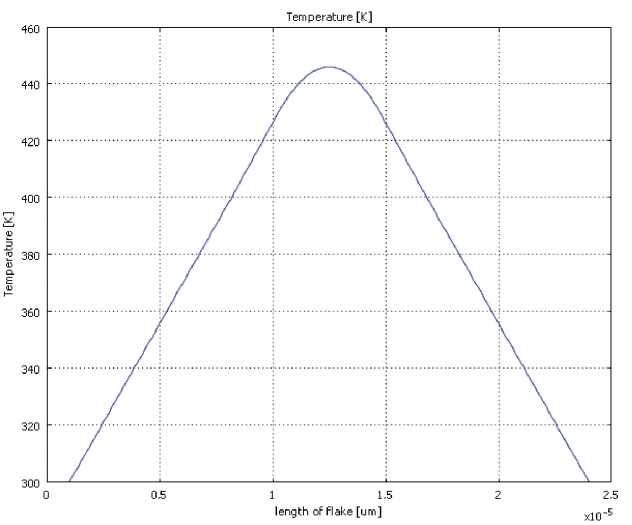

Fig. 19. Local temperature as a function of the coordinate along the large symmetry axis. Disk heat source with a diameter of 5 μm.

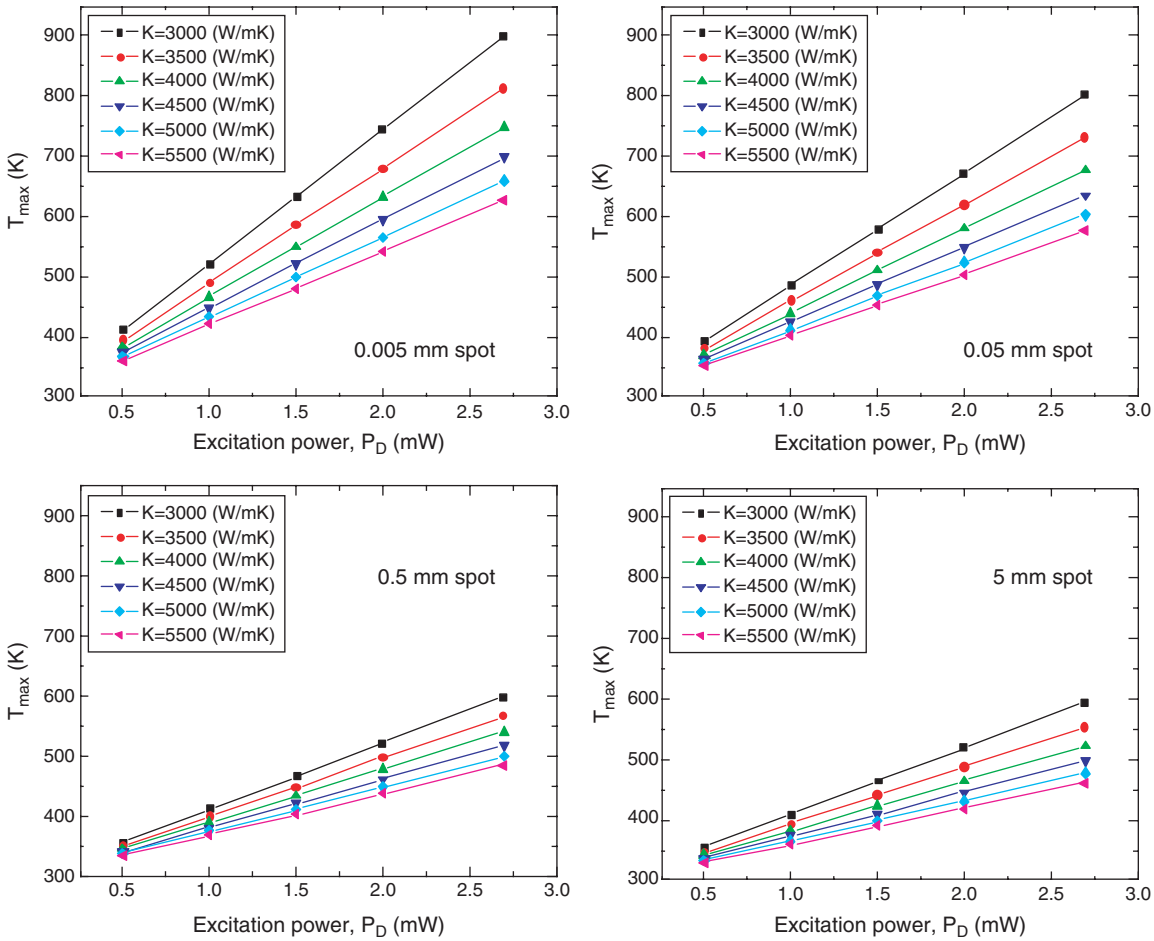

Fig. 20. Temperature at the center of the laser spot (disk source) as a function of the detector power for different values of graphene's thermal conductivity and different diameters of the laser spots.

source as a disk with a distinct boundary can be replaced by the model of the heat source where the power follows Gaussian distribution. We considered two somewhat extreme cases. In the first case we assumed that, if the detector power distribution is normal, then the peak of the distribution equals the power in the model of the disk source (i.e., 2 mW). We looked what the maximum temperature and the expected thermal conductivity would be if the sigma σ of the Gaussian equals half or one-third of the radius in the disk heat source model when the disk diameter equals 0.5 μm. The results are shown in Table VII.

When $2\sigma = R$, both the maximum temperature (measured under the condition that the thermal conductivity of graphene equals $k = 5000$ $\mathrm{Wm^{-1}K^{-1}}$) and expected

Table VI. Maximum temperatures and expected thermal conductivities for different sizes of the hot disk source. Shape 1 is considered. T_{max} is the maximum temperature when the excitation power is $P_D = 2$ mW and the thermal conductivity of graphene is $k = 5000$ $\mathrm{Wm^{-1}K^{-1}}$; $T_{0.5\_max}$ is the maximum temperature when the excitation power is $P_D = 2$ mW, the thermal conductivity of graphene is $k = 5000$ $\mathrm{Wm^{-1}K^{-1}}$ and the laser spot diameter is 0.5 μm; k is the expected thermal conductivity of graphene when $\theta = 1.226$ $\mathrm{cm^{-1}(mW)^{-1}}$; $k_{0.5}$ is the expected thermal conductivity of graphene when $\theta = 1.226$ $\mathrm{cm^{-1}(mW)^{-1}}$ and the laser spot diameter is 0.5 μm.

Spot diameter, μm	T_{max} (K)	$T_{max}/T_{0.5\_max}$ (%)	k ($\mathrm{Wm^{-1}K^{-1}}$)	$K/K_{0.5}$ (%)
0.5	477.72	100	5816.80	100
0.005	566.03	118.49	8697.63	149.53
0.05	523.79	109.64	7310.93	125.69
5	431.39	90.30	4303.94	73.99

Table VII. Maximum temperatures and expected thermal conductivities for different sigmas of Gaussian heat source. Shape 1 is considered. T_{max} is the maximum temperature when the thermal conductivity of graphene is $k = 5000$ $\mathrm{Wm^{-1}K^{-1}}$; $T_{0.5\_max}$ is the maximum temperature when the disk heat source is used, the excitation power is $P_D = 2$ mW and the thermal conductivity of graphene is $k = 5000$ $\mathrm{Wm^{-1}K^{-1}}$ and the laser spot diameter is 0.5 μm; k is the expected thermal conductivity of graphene when $\theta = 1.226$ $\mathrm{cm^{-1}(mW)^{-1}}$; $k_{0.5}$ is the expected thermal conductivity of graphene when $\theta = 1.226$ $\mathrm{cm^{-1}(mW)^{-1}}$ and the disk source is used with the laser spot diameter 0.5 μm.

Sigma measured in $R = 0.25$ μm	T_{max}(K)	$T_{max}/T_{0.5\_max}$ (%)	k ($\mathrm{Wm^{-1}K^{-1}}$)	$k/k_{0.5}$ (%)
$R = 2\sigma$	390.05	87.74	2955.19	62.00
$R = 3\sigma$	341.73	76.87	1394.69	29.26

thermal conductivity are reasonably close to the reported values (the expected thermal conductivity is closer to the lower experimental bound). But, when $3\sigma = R$, both the maximum temperature and expected thermal conductivity demonstrate the values significantly lower than the values reported by the experiment.

In the second case we assumed that the volume integral of the laser power, which follows the Gaussian distribution, equals the volume integral of the power in the model of the disk heat source. Both volume integrals can be computed using polar coordinates r, θ and z:

$$\int_0^\infty P_{\text{peak}} e^{-(r^2/(2\sigma^2))} r\,dr \int_0^{2\pi} d\theta \int_0^h dz = \int_0^R Pr\,dr \int_0^{2\pi} d\theta \int_0^h dz \quad (38)$$

where $R = 0.25$ mm is the radius of the spot in the disk heat source model, $P = 2$ mW is the power of the detector in the disk source model, P_{peak} is the peak power of the detector in the Gaussian heat source model.

We studied the case when $\sigma = R/3$. Solving the Eq. (38) allows one to find the peak power P_{peak}, which approximately equals 4.5 mW. Then we found that the maximum temperature (assuming the thermal conductivity of graphene equals $k = 5000$ $\text{Wm}^{-1}\text{K}^{-1}$) and the expected thermal conductivity of the flake are equal to 487.78 K and 6136.99 $\text{Wm}^{-1}\text{K}^{-1}$, correspondingly. As it is seen, in this model the expected thermal conductivity exceeds the reported values.

7. SUMMARY

It was also recently reported[14, 15] that graphene is an excellent conductor of heat with the room temperature thermal conductivity values on the order of or exceeding those of carbon nanotubes. The measurements of thermal conductivity of graphene utilized a non-contact optical technique where the excitation laser initiated a heat wave propagating through graphene flake toward the heat sinks. The experimental data extraction procedure assumed a plane heat wave front. Realistic graphene flakes have variation in their width, and the heat wave front may deviate from the plane wave depending on the geometry of the flake and ratio of the laser-spot diameter and the flake width. In this work we performed detail simulation study of heat propagation in graphene flakes of various shapes. The simulations were carried out using the finite-element method with the help of the COMSOL software. The structure parameters, heat sources and boundary conditions were selected to closely correspond to those reported in the experiments.[14, 15] The generated fine meshes allowed us to study heat conduction with high accuracy and obtain accurate temperature profiles. We focused on the effects of the shape of the flake on the obtained value of thermal conductivity for the fixed amount of the dissipated power in the middle of the suspended graphene.

It was found that both the shape of the flake and the selected temperature distribution in the hot spot (liner source vs. point source; uniform vs. Gaussian) affect the extracted values of thermal conductivity. At the same time, for the flakes with the relatively constant width and the hot spot of the size comparable to the flake width, the thermal conductivity extracted within the simple plane-wave approximation give close values to our simulation results. The very high values of the thermal conductivity of graphene, in excess of ~3000 W/mK, are beneficial for the electronic and thermal management applications of graphene. It is also interesting to point out that carbon-based materials, depending on their atomic structure and amount of disorder, can be both exceptional thermal conductors, like graphene and carbon nanotubes, and thermal insulators, like amorphous diamond or diamond-like carbon.[18, 19] The developed simulation procedure can be further used for investigation of thermal transport in graphene multi-layers and graphene–heat sink structures. The latter is required in order to assess the feasibility of application of graphene multi-layers for the lateral hot-spot removal and other device-level thermal management applications.[20] Due to the increasing dissipation power density, switching speed and thermal resistance of the multi-layer structures, the device-level thermal management becomes important not only for conventional electronics but also for magnetic memory,[21] logic elements with alternative state variables,[22] three-dimensional and reconfigurable architectures[23] and optoelectronic devices.[24]

Acknowledgments: We thank Professor A. A. Balandin (UCR) for drawing our attention to this problem and providing experimental data for comparison with the simulations. This work was supported, in part, by the Focus Center Research Program (FCRP) through its Center on Functional Engineered Nano Architectonics (FENA).

References and Notes

1. K. S. Novoselov, A. K. Geim, S. V. Morozov, D. Jiang, Y. Zhang, S. V. Dubonos, I. V. Grigorieva, and A. A. Firsov, *Science* 306, 666 (**2004**).
2. A. K. Geim and K. S. Novoselov, *Nature Mater.* 6, 183 (**2007**).
3. A. Jorio (ed.), Carbon Nanotubes: Advanced Topics in the Synthesis, Structure, Properties and Applications, Springer-Verlag, Berlin/Heidelberg (**2008**).
4. J. H. Chen, C. Jang, S. Xiao, M. Ishigami, and M. S. Fuhrer, *Nature Nanotech.* 3, 206 (**2008**).
5. A. B. Kuzmenko, E. van Heumen, F. Carbone, and D. van der Marel, *Phys. Rev. Lett.* 100, 117401 (**2008**).
6. R. R. Nair, P. Blake, A. N. Grigorenko, K. S. Novoselov, T. J. Booth, T. Stauber, N. M. R. Peres, and A. K. Geim, *Science* 320, 1308 (**2008**).
7. I. W. Frank, D. M. Tanenbaum, A. M. van der Zande, and P. L. McEuen, *J. Vac. Sci. Technol. B* 25, 2558 (**2007**).
8. N. D. Mermin and H. Wagner, *Phys. Rev. Lett.* 17, 1133 (**1966**).
9. S. Coleman, *Comm. Math. Phys.* 31, 259 (**1973**).
10. A. Klein, L. J. Landau, and D. S. Shucker, *J. Stat. Phys.* 26, 505 (**1981**).

11. J. C. Meyer, A. K. Geim, M. I. Katsnelson, K. S. Novoselov, T. J. Booth, and S. Roth, *Nature* 446, 60 **(2007)**.
12. K. S. Novoselov, A. K. Geim, S. V. Morozov, D. Jiang, M. I. Katsnelson, I. V. Grigorieva, S. V. Dubonos, and A. A. Firsov, *Nature* 438, 197 **(2005)**.
13. Y. Zhang, Y.-W. Tan, H. L. Stormer, and P. Kim, *Nature* 438, 201 **(2005)**.
14. A. A. Balandin, S. Ghosh, W. Bao, I. Calizo, D. Teweldebrhan, F. Miao, and C. N. Lau, *Nano Lett.* 8, 902 **(2008)**.
15. S. Ghosh, I. Calizo, D. Teweldebrhan, E. P. Pokatilov, D. L. Nika, A. A. Balandin, W. Bao, F. Miao, and C. N. Lau, *Appl. Phys. Lett.* 92, 151911 **(2008)**.
16. I. Calizo, A. A. Balandin, W. Bao, F. Miao, and C. N. Lau, *Nano Lett.* 7, 2645 **(2007)**; I. Calizo, F. Miao, W. Bao, C. N. Lau, and A. A. Balandin, *Appl. Phys. Lett.* 91, 071913 **(2007)**; I. Calizo, W. Bao, F. Miao, C. N. Lau, and A. A. Balandin, *Appl. Phys. Lett.* 91, 201904 **(2007)**.
17. See description at http://www.comsol.com.
18. W. L. Liu, M. Shamsa, I. Calizo, A. A. Balandin, V. Ralchenko, A. Popovich, and A. Saveliev, *Appl. Phys. Lett.* 89, 171915 **(2006)**; M. Shamsa, S. Ghosh, I. Calizo, V. Ralchenko, A. Popovich, and A. A. Balandin, *J. Appl. Phys.* 103, 083538 **(2008)**.
19. M. Shamsa, W. L. Liu, A. A. Balandin, C. Casiraghi, W. I. Milne, and A. C. Ferrari, *Appl. Phys. Lett.* 89, 161921 **(2006)**; A. A. Balandin, M. Shamsa, W. L. Liu, C. Casiraghi, and A. C. Ferrari, *Appl. Phys. Lett.* 93, 043115 **(2008)**.
20. A. A. Balandin, E. P. Pokatilov, and D. L. Nika, *J. Nanoelectron. Optoelectron.* 2, 140 **(2007)**; A. A. Balandin, *J. Nanosci. Nanotechnol.* 5, 7 **(2005)**.
21. R. Ikkawi, N. Amos, A. Lavrenov, A. Krichevsky, D. Teweldebrhan, S. Ghosh, A. A. Balandin, D. Litvinov, and S. Khizroev, *J. Nanoelectron. Optoelectron.* 3, 44 **(2008)**.
22. A. Khitun, M. Bao, J.-Y. Lee, K. L. Wang, D. W. Lee, S. X. Wang, and I. V. Roshchin, *J. Nanoelectron. Optoelectron.* 3, 24 **(2008)**; V. V. Zhirnov and R. K. Cavin, *J. Nanoelectron. Optoelectron.* 1, 52 **(2006)**.
23. J.-P. Wang and X. Yao, *J. Nanoelectron. Optoelectron.* 3, 12 **(2008)**.
24. A. I. Yakimov, A. V. Dvurechenskii, and A. I. Nikiforov, *J. Nanoelectron. Optoelectron.* 1, 119 **(2006)**; M. A. Makeev, *J. Nanoelectron. Optoelectron.* 1, 176 **(2006)**.

Received: xx Xxxx xxxx. Revised/Accepted: xx Xxxx xxxx.